STARS

University of Central Florida
STARS

Electronic Theses and Dissertations, 2004-2019

2009

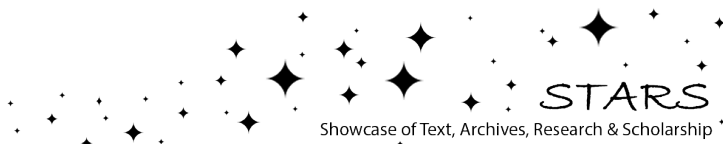# Water Vapor And Carbon Dioxide Species Measurement In Narrow Channels

Derek Lambe
University of Central Florida

Part of the Aerospace Engineering Commons

Find similar works at: https://stars.library.ucf.edu/etd

University of Central Florida Libraries http://library.ucf.edu

This Masters Thesis (Open Access) is brought to you for free and open access by STARS. It has been accepted for inclusion in Electronic Theses and Dissertations, 2004-2019 by an authorized administrator of STARS. For more information, please contact STARS@ucf.edu.

University of Central Florida

STARS
Showcase of Text, Archives, Research & Scholarship

www.manaraa.com

WATER VAPOR AND CARBON DIOXIDE SPECIES
MEASUREMENT IN NARROW CHANNELS

by

DEREK EDWARD LAMBE
B.S. University of Central Florida, 2007

A thesis submitted in partial fulfillment of the requirements
for the degree of Master of Science
in the Department of Mechanical, Materials, and Aerospace Engineering
in the College of Computer Science and Engineering
at the University of Central Florida
Orlando, Florida

Summer Term 2009

© 2009 Derek Lambe

ABSTRACT

A novel method has been implemented for measuring the concentration of gas species, water vapor and carbon dioxide, within a narrow channel flow field non-invasively using tunable diode laser absorption spectroscopy (TDLAS) in conjunction with a laser modulated at a high frequency [Wavelength Modulation Spectroscopy (WMS)] tuned to the ro-vibrational transition of the species. This technique measures the absorption profile which is a strong function of the species concentration across short path lengths and small time spans, as in PEM fuel cells during high load cycles. This method has been verified in a transparent circular flow 12 cm path length and a 12 mm rectangular flow channel. Distinct absorption peaks for water vapor and carbon dioxide have been identified, and concentrations of water vapor and carbon dioxide within the test cells have been measured in situ with high temporal resolutions. A comparison of the full width at half maximum (FWHM) of the absorption lineshapes to the partial pressure of water vapor and carbon dioxide showed a predominantly linear relationship, except in the lower partial pressure regions. Test section temperature was observed to have very minimal impact on these curves at low partial pressure values. A porous media like a membrane electrode assembly (MEA) similar to those used in PEM fuel cells sandwiched between two rectangular flow channels was also tested. Some of the scattered radiation off the MEA was observed using a photodiode at high gain, allowing for more localized species detection. The technique was used to monitor the humidity on either side of the MEA during both temperature controlled and super-saturated conditions. The measurements were observed to be repeatable to within 10 %.

TABLE OF CONTENTS

LIST OF FIGURES

LIST OF TABLES

NOMENCLATURE

A_{Mod}	amplitude of modulation
FWHM	full-width at half-maximum
HWHM	half-width at half-maximum
$\bar{I}_0$	average injection current
i_0	injection current modulation amplitude
$I_0(t)$	laser output intensity
m	modulation depth
t	time

GREEK SYMBOLS

α	wavelength modulation amplitude
ν(t)	laser frequency
$\bar{\nu}$	average wavelength
Ψ	phase shift
ω	modulation frequency

CHAPTER ONE: INTRODUCTION

As technology advances, the scale of fluid mechanics applications continues to shrink. A majority of today's fluids mechanics research capital is invested in the study and development of fluid flow on the mini, micro, and nano levels. The importance of small scale phenomena such as pool boiling in small hydraulic diameter channels is on the rise for many diverse applications [1]. The ability to reliably and non-invasively detect the bubble size and vapor concentration in pool boiling could assist in measuring the heat transfer rates involved. Another much studied topic in the field of pool boiling has been the effect of dissolved gases (particularly air and CO_2 [2, 3]) on the heat transfer rates. As the fluid is heated, the solubility of the gases change and desorption may occur, causing apparent nucleate boiling to begin at a different temperature [4]. Non-intrusive species concentration measurements within the resulting bubbles could provide better insight to these effects.

Reactor/reactant species concentration detection in microscale chemical reactors is another important research topic. In these reactors, the reacting species undergo a chemical change resulting in the production of heat and reactant species. The water gas shift (WGS) reactor described by Tonkovich et al [5] converts carbon monoxide and steam into carbon dioxide and hydrogen as part of the process for generating hydrogen from conventional fuel for use in fuel cell applications [5]. Because of its small size (with hydraulic flow diameters < 5 mm and channel lengths from 1-10 cm), most conventional diagnostic equipment would be too costly or too invasive to employ. The development of a non-invasive and cost efficient means of in-situ species detection to monitor such reactors could lead to further enhancements in efficiency.

1

The development of compact power sources for portable electronics is another field which could benefit greatly from improvements in non-invasive species detection. As reported by Epstein [6], millimeter-scale micro-electro-mechanical systems (MEMS) gas turbine engines are currently being developed for applications requiring higher energy densities than traditional lithium battery chemistry can provide [6]. These devices utilize flow channels and combustion chambers with hydraulic diameters ranging from approximately 1-3 mm. A system to monitor fuel/air mixing and reactant formation in an active turbine could provide more insight into system efficiency and grant researchers a better understanding of how it could be improved. Other MEMS applications that could also benefit from non-intrusive species concentration measurements include micro motor driven compressors [7] and micro-bipropellant rocket motors [8].

One particular application which has been the motivation behind this study is species monitoring within the flow channels of proton exchange membrane (PEM) fuel cells. The concentrations of the fuel and byproduct species in the narrow (< 4 mm wide) flow channels of a PEM fuel cell have been observed to impact the energy production levels of the cell. Water vapor has been shown to have a distinctly strong impact on the protonic conductivity of the membrane, with the most common membrane material, Nafion$^{©}$, exhibiting an order of magnitude increase in conductivity with a rise in relative humidity from 35 to 85% [9]. Because of the production of water in cathode reactions and the various transport processes known to take effect in an operational cell (i.e. electro-osmotic drag and diffusion due to pressure gradients), the distribution of water within the cell is often non-homogeneous [10, 11]. This non-homogeneous distribution can lead to localized flooding or dehydration of the membrane, resulting in a significant drop in cell performance. An understanding of the effect of operational

2

conditions on the temporal concentration gradient of water along the cell flow channels, especially during high frequency load cycles, could provide greater insight into the water transport processes and lead to further developments in cell design and control systems.

Carbon dioxide is another species which must be given consideration in PEM fuel cell power generation. To integrate such fuel cells into mainstream applications such as automobiles in an expedient manner, it would be necessary to operate them on fuels which could be distributed using current infrastructure. Such fuels (i.e. syngas) often contain up to 25% carbon dioxide. While regarded as relatively inert in its native state, studies have suggested that the molecule may give up an oxygen atom to adsorbed hydrogen in the system through the process of a reverse water-gas shift reaction, producing carbon monoxide and thus poisoning the membrane and reducing cell efficiency [12]. Chemical degradation of the membrane has also been shown to produce CO_2 [13]. The ability to monitor the temporal history of CO_2 concentration throughout the cell could both allow for a greater understanding of the nature of the negative impact the gas has on cell efficiency and provide an indicator as to the conditions under which chemical degradation occurs.

As indicated by Faghri and Guo [14], a number of attempts have been made to model the mass transfer and species flow processes within an operational PEM fuel cell. These studies have used various computational parameters to simulate flow, ranging from 1-D theoretical computation for two phase flow [15] to numerical 2-D [16] and 3-D models for both one [17] and two phase [18, 19] flows. In order to validate these models, experimental measurements must be obtained from actual cells in a non invasive manner. Most previous attempts to measure species concentration within operational fuel cells in a non-invasive manner have been conducted using gas samples from the inlet and outlet of the cell. With these samples,

3

measurement techniques such as gas chromatography [20, 21], Fourier transform infrared spectroscopy [22], and chilled mirror hygrometry [23] have been implemented. Unfortunately, to employ such tests in an attempt to gather localized data would require the invasive extraction of gas samples from the cell, decreasing the integrity of the experiment. Non-invasive imaging techniques such as neutron scattering [24, 25, 26] and X-ray scattering [27] have been implemented to study the localized spatial distribution of hydration states, but these techniques are somewhat impractical as they require the cell to be mounted within large and expensive pieces of equipment which are not readily available. Numerous visual studies have also been performed such as that conducted by Borrelli et al [28]. In this study, a high speed camera was used to observe water droplet formation through the gas diffusion layer (GDL) of a simulated PEMFC. While such visual studies provide a wealth of information on liquid water transport, they cannot provide data on species concentrations such as CO_2 and water vapor.

In a series of studies conducted by Basu et al [29, 30, 31], tunable diode laser absorption spectroscopy (TDLAS) was introduced as a practical and truly non-invasive means of determining localized species concentration and gas temperature. In these studies, the concentration and temperature of water vapor along several of the flow channels within an operating PEM fuel cell were measured for both steady state and dynamic load conditions. This method is limited, however, by relatively long scan times (upwards of four seconds) and a high sensitivity to noise, thus preventing its application to high frequency load cycles or species with relatively weak IR transitions (like CO_2) or extremely small concentration.

The work detailed in this paper both seeks to expand upon the traditional TDLAS method by using wavelength modulation and to apply the technique to study water transport across an MEA in a localized manner. The theory behind WMS measurements is discussed in more detail

later in this paper. The experimental data reported in the subsequent sections serve as a proof of concept for WMS detection of the species concentrations of water vapor and carbon dioxide along short path lengths, particularly those similar to lengths common in PEM fuel cell flow channels.

It should be noted that the use of TDLAS and WMS for detection of species concentration has been in existence for a number of years. However, the novelty can be found in its application to the PEM fuel cell and mini-channel environment. The unique combination of TDLAS and WMS is necessary to make laser measurements through the narrow space of the cell with greater temporal and spatial resolution.

CHAPTER TWO: EXPERIMENTAL APPROACH

In the current experiment, wavelength modulation spectroscopy was used to measure water vapor and carbon dioxide second harmonic absorption profiles as a function of excitation wavelength. An optically accessible test cell was constructed in order to test the applicability of this method to a short path length. To create the test cell, a copper tube of 1cm ID was capped on each end with BK7 optical glass and 2 cm of 'dead space'. The resulting active path length of the cell was measured to be 12 cm. In order to avoid etalon interference (back reflection of the incident laser light), the glass windows were attached to each end at a slight angle. Cell temperature was monitored via a thermocouple inserted near the gas inlet. In case of short path length measurements (both direct and MEA scattered techniques), the copper test cell was replaced by a 12 mm long acrylic cell. Temperature for the acrylic cell was monitored using thermocouples on both the inner and outer channel walls. These test sections were designed to emulate the short path lengths commonly found in minichannel applications like the fuel cell gas channels.

Measurements for each of the species were conducted independently. Results were obtained for each of the following cases:

Water vapor concentration along a 12cm path length

Water vapor concentration across the 12mm depth of a channel

Water vapor concentration across the 12mm depth of a channel using MEA scattering

Carbon dioxide concentration along a 12cm path length

In each instance, the output from the appropriate distributed feedback (DFB) diode laser was collimated using a wavelength adjustable collimator (ThorLabs CFC-11-C) to produce a

beam-spot size of roughly 1 mm [reducible to 0.5 mm] and passed along the length of the cell for each of the above conditions. While such a small beam size was not necessary given the relatively large diameter of the cell, future application of the technique would be within much narrower passages, the overall size of which would only be limited by beam collimation. In order to limit the influence of atmospheric conditions outside the cell, the collimator was shielded and placed close to the glass to minimize such effects.

In order to tune the laser wavelengths across the desired transitions, temperature and current control were implemented. Each laser was mounted within a butterfly laser mount (ThorLabs LM14S2) and controlled using a laser diode and temperature controller (ThorLabs ITC510). This allowed for both course wavelength control via temperature adjustment and rapid fine tuning through current modulation. The current was controlled using the output from a data acquisition system (NI PCI-MIO-16-E) and was modulated at high frequencies and swept across various wavelengths depending upon the transition of the species being measured.

The DFB laser diode used for water vapor (NEL NLK1S5GAAA) was swept across 0.17 nm about the ro-vibrational transition located at 1491.416 nm. Initially, direct absorption spectroscopy was performed to validate the chosen transition profile with the spectroscopic simulations using HITRAN database. Next, WMS was conducted, in which the current was modulated at 5 kHz and ramped at a frequency of 10 Hz for a total of five scans, resulting in a total scan time of 0.5 seconds. To obtain first harmonic absorption profiles for comparison with spectroscopically simulated profiles (HITRAN), a modulation depth of roughly 0.1 was employed. To obtain the desired second harmonic profiles, a modulation depth of roughly 1 was used.

7

The DFB laser diode used for carbon dioxide (NEL NLK1556STG) was swept across 0.14 nm about the transition located at 1571.4 nm. The current was modulated at 60 kHz and ramped at a frequency of 4 Hz for 10 iterations, resulting in a total scan time of 2.5 seconds. Current amplitude was modulated at a depth similar to that used for the water vapor second harmonic profiles. Both lasers were calibrated for wavelength using an optical spectrum analyzer. The power of each attenuated beam after passing through the cell was monitored using an InGaAs amplified photodetector (ThorLabs PDA10CS).

In order to remove ambient noise from the signal and provide the first and second harmonic absorption profiles, the photodetector was connected to a digital signal processing (DSP) lock-in amplifier (Scitec 450S). The response time constant for the amplifier was set between 1 ms and 5 ms depending on the profile being measured. A gain was also applied during post-amplification depending upon the signal strength. A function generator was used to provide a reference signal, allowing the lock-in amplifier to isolate a desired frequency within the observed signal. By setting the reference signal equal to the modulation frequency, the first harmonic profile was measured. The second harmonic profile was obtained by providing a reference signal at twice the modulation frequency.

Conditions within the cell were controlled by using heat tapes, insulation and a humidifier/mixing tank. The cell, tank, and connecting pipe were wrapped in heat tape and insulated. Temperatures within the cell and tank were independently controlled using temperature controllers (Dwyer 16B-33) and strategically placed J type thermocouples. The tank consisted of a pipe, sealed at both ends, with three swagelok ports, two open and one attached to an internal sting. When water vapor was required, the tank was filled most of the way with water. The open ports served to connect the tank to the cell and to allow for visualization of

8

water level. The tank was heated to a desired temperature and air was forced through the sting using an air compressor. The bursting bubbles caused the air leaving the tank to become saturated, with exit hygrometer measurements confirming the relative humidity (at tank temperature) to be within 2 % of total saturation. During carbon dioxide measurements, CO_2 was forced through the sting while air from an air compressor was fed through one of the open ports. This provided for better homogeneous mixing at desired volume percentage of CO_2 to occur before the gas passed through the remaining open port and the cell. A schematic of the experimental setup is shown in Figure 1.

MEA backscatter measurements were conducted in a fashion somewhat similar to that described by Fujii et al [33]. In order to conduct the measurements, the MEA employed (Fuel Cell Scientific 50cm^2 MEA .5mg Pt/cm^2 Nafion 115) was sandwiched between two 12 mm deep acrylic flow channels. Humid air was supplied to one channel while dry air was passed through the other at a similar flow rate. The laser was passed through the acrylic window at a slight angle to reduce the chance of etalon interference as well as to direct the backscatter at a convenient angle for detection with the photodiode. To obtain a calibration curve for the backscattered measurements, a laminate sheet was placed between the MEA and the humid channel to prevent water transport and measurements were taken using known partial pressure values of water vapor. A schematic of this setup can be seen in Figure 2A. After calibration was completed, the laminate material was removed and the technique was verified using a heated test cell (Figure 2B). Finally, measurements were taken on both sides of the MEA under super-saturated and unheated conditions. A diagram of this test section can be seen in Figure 2C.

9

2.1 Wavelength Modulation Spectroscopy

In a procedure similar to traditional TDLAS measurements (direct absorption), in WMS, a laser beam is passed through a gas sample and scanned across a frequency band coinciding with certain ro-vibrational transitions of the species to be measured. Through the implementation of wavelength modulation spectroscopy, a desired absorption signal is separated from the standard levels of noise, allowing for the detection of signal characteristics which would normally be lost because of their small amplitude. To accomplish this, the driving signal (containing the water vapor or CO_2 species signature) is modulated at a certain amplitude (modulation depth) and a high frequency (tens of kHz) and the resulting absorption signal is analyzed using a lock-in amplifier. Functioning as both an amplifier and a phase sensitive detector (PSD), the lock-in amplifier multiplies the incoming signal by a phase locked reference sine wave at the desired frequency, allowing the PSD component of the amplifier to act as a band-pass filter with a very narrow bandwidth (as low as 0.01 Hz). This isolates the signal from much of the normally present noise. After being processed by the lock-in, the signal represents an amplified root mean squared (RMS) voltage for the sinusoidal signal detected at the reference frequency. In the case of complex signals, the processed signal will be representative of the Fourier transform of the signal at the harmonic referenced.

To achieve the modulated laser output required for the implementation of WMS, the current of the laser is driven using a high frequency sinusoidal signal and a slowly varying ramp. Under these conditions, the laser frequency, *v(t),* and output intensity $I_0(t)$ can be expressed as

$$v(t) = \bar{v} + a\cos(\omega t) \qquad (1)$$

10

$$I_0(t) = \bar{I}_0 + i_0 \cos(\omega t + \psi) \qquad (2)$$

In this case, $\bar{v}$ and $\bar{I}_0$ are representative of the slowly varying average values for the wavelength and injection current respectively. The modulation amplitudes are given by a and i_0 while the modulation frequency is described by ω. Ψ describes the phase shift between the laser frequency and intensity that results from high modulation frequencies. For DFB lasers, the phase shift commonly lies somewhere between 0 and $-\pi$, decreasing with increasing frequency [34].

When the modulated laser beam is passed through an absorptive medium, the interaction of the modulated laser frequency with the absorption feature will lead to a fluctuation in laser intensity. This fluctuation results not only in a variation in signal amplitude, but also makes the signal complex. In the region of the absorption feature, harmonic frequencies are generated and can be isolated with the lock-in amplifier. The properties of these harmonic features are influenced by the amplitude of the signal modulation, often referred to in terms of modulation depth m:

$$m = \frac{A_{Mod}}{HWHM} \qquad (3)$$

where HWHM is the half-width at half-maximum of the absorption feature being observed.

When the modulation depth is small ($m \ll 1$), the harmonic absorption profiles are nearly equal to the comparative derivatives of the direct absorption signal (i.e. the first harmonic signal is representative of the first derivative, the second harmonic signal is representative of the second derivative, etc.). This is useful when comparing the observed absorption signal to

11

spectroscopically simulated profiles generated using data from HITRAN. As the modulation depth is increased, the harmonic absorption profiles become broadened and their intensities change. It has been shown that in most cases, the intensity peaks in the area of $m \sim 2.2$ [34]. This is ideal for most applications, especially when the desired signal is weak. For even greater modulation depths, broadening becomes the prominent feature and resemblance to the derivative of the original profile is lost.

2.2 Wavelength Selection

One of the key procedures which must be implemented prior to the use of any type of TDLAS application is selection of the appropriate transition wavelength for the desired species. In order to achieve accurate and reliable concentration measurements, it is of critical importance that the selected transition be isolated from any strong absorption lines for any of the other gasses which may be present within the system. The intensity of the absorption is another important factor to consider, especially when working with small path lengths, as larger absorptions will be more readily observable. Other selection criteria may be included, depending on the scope of the experiment. In the case of this study, it was desirable to use relatively inexpensive and readily available laser components. Because of the vast amount of research and development conducted by the telecommunications industry, components operating in the near infrared range between 1400 and 1600 nm were the most attractive choice. Another important consideration of this study was the influence of system temperature on pressure and Doppler broadening. Doppler broadening is an effect of thermal induced motion of the molecules of the measured gas species and is thus governed entirely by system temperature. Pressure broadening occurs because of the interaction of the observed molecules with other molecules within the

12

system. This effect is influenced not only by system temperature, but also by the density of the gasses involved and thus the partial pressure of the measured species. To reduce the impact of system temperature on the target parameter of the measurement (the full-width at half-maximum of the second harmonic absorption profile), it was desirable to select a transition with low thermal influence in the range of temperatures common to PEM fuel cell operation (60-100°C).

To begin the selection process for water vapor, the HITRAN database was used to create a plot of the absorption intensity for all gaseous H_2O transition lines in the 1400 to 1600 nm region. This graph can be seen in Figure 3. Though particularly strong absorptions can be observed in the wavelengths closer to 1400 nm, there was found to be less isolation from other species such as CO and CO_2. Further investigation revealed the region around 1491 nm to be sufficiently isolated. Absorption intensities in this region were observed in detail (Table 1) and a particularly strong band was selected at 1491.416 nm. Finally, absorption profiles were simulated using the HITRAN data for the desired temperature range to observe the effects of system temperature on broadening. The simulated profiles can be seen in Figure 4.

A similar procedure was used to identify a desirable transition for CO_2. The resulting wavelength selected was 1571.406 nm. Data for the transition intensities in this region can be found in Table 2.

2.3 LabView Programming

In order to control the experiment, it was necessary to code a LabView program capable of simultaneous output of control values and input of resulting data. The block diagram for the program coded to meet these conditions can be seen in Figure 5. In this program, the output values for control of the laser diode are first generated by summing a ramp and a high frequency

sine function. The resulting function is then passed to a graphical display on the user interface for verification and to a for loop where it is output to the laser diode controller. Samples are simultaneously taken from the input (either from the photodiode directly, or from the lock-in amplifier) and passed to a feedback loop where the data from each iteration is summed. After the feedback loop, the data is divided by the current iteration to create an averaged profile which is output to the graphical display on the user interface and passed to an 'output to file' function. This function creates a file containing the data supplied during the final iteration for later processing. An image of the graphical user interface can be seen in Figure 6. From this display, the user can control the maximum and minimum output and input values, as well as the total iterations for each scan. To modify other parameters such as output function and sampling rates, the user must make adjustments within the block diagram.

In order to maintain consistent selection practices for the FWHM of each plot, as well as to expedite the process, a second LabView program was created to take the measurement. The block diagram for this program can be seen in Figure 7. After reading data from the user selected input file and identifying the central peak under the given parameters, the program would calculate the half-maximum using the peak value and the smallest value present in the data. Using this value and an algorithm for determining duration, the program would then output the total scan time which elapsed between the half-max values. If the range of wavelengths swept is supplied by the user, the program will also supply the FWHM in terms of wavelength. An image of the graphical interface for this program can be seen in Figure 8. From this interface, the user can select the input file, set the parameters for determination of the central peak, and indicate a total wavelength range for the scan. The profile contained in the selected

14

data file is displayed on the interface to allow the user to easily determine the parameters necessary for central peak detection.

CHAPTER THREE: RESULTS AND DISCUSSION

In this section of the paper, the results for the calibration of the second harmonic detection technique for measuring water vapor and carbon dioxide along short path lengths using known gas concentrations are reported. Test section temperatures were varied [60 - 100°C] as part of a parametric study, with temperature selections similar to those which can be found in operational PEM fuel cells. In each case, the measurements were taken after allowing the system to reach steady-state flow conditions to ensure species concentration accuracy. Carbon dioxide species concentrations were observed along the length of a short channel (12 cm) in order to simulate a measurement along the length of a flow channel in an operational PEM fuel cell or similar mini-channel application. Water vapor concentrations were measured across the depth (12 mm) of a similar channel under various temperature conditions. In the next section, a proof of measurement repeatability will be presented first, along with a HITRAN comparison for measurement validation. This will be followed by the results for the water vapor measurements. The section will conclude with the results for the carbon dioxide measurements.

3.1 HITRAN Comparison

In order to validate the TDLAS measurement method as well as the chosen absorption profile for water vapor, several direct absorption and first harmonic absorption profiles were recorded. These profiles were then compared to profiles generated mathematically using information from the HITRAN database. Figure 9A compares a direct absorption profile for a cell temperature of 80°C and water vapor partial pressure of 0.062 atm to the simulated profile

16

generated using similar parameters. Figure 9B compares a first harmonic absorption profile measured for the same temperature and a partial pressure of 0.055 atm and its matching simulated profile. The first harmonic absorption profile was generated using a small modulation depth in order to more accurately represent the numerical derivation on which the simulated profile is based. The measured profiles are seen to match quite well with the simulations.

3.2 Repeatability of Measurements

Key objective in designing a measurement system is to ensure that the results reported are consistent and repeatable. Such is the case when utilizing WMS/direct absorption to determine species concentration. As the strength of an absorption profile is primarily dependent upon a number of controllable parameters (species concentration, alignment, cell temperature, gain, modulation depth, etc.), it is expected that the level of repeatability should be high. Under identical measurement conditions, the measured profiles should also be nearly identical. In Figure 4A and 4B, a number of repeated measurements for water vapor and carbon dioxide concentrations (respectively) are shown. These measurements were conducted using identical cell temperature, alignment, and instrument settings for each species concentration while allowing for a considerable time lapse between measurements. It can be seen readily that, in each case, the profiles are nearly identical. The small observable deviations are predominantly confined to the sidebands. This suggests a high degree of repeatability, as was expected given the nature of the measurement.

Figure 10A displays the results of water vapor measurements along the 12 mm test path for two different species concentrations, each repeated three times. The cell temperature was

17

maintained at 80°C (±1°C). The partial pressures used in these measurements (0.073 atm and 0.197 atm) resulted in test cell relative humidities of 15.7 and 42.4 %. The second set of measurements, seen in Figure 10B, was taken for carbon dioxide along the 12 cm test path at room temperature. The measurements were repeated for 80%, 20%, and 10% carbon dioxide by volume. Further measurements have shown these presented cases to be representative of measurement repeatability under any given set of conditions.

It should be noted that changes in laser alignment or system gain could result in increased/decreased absorption intensity and thus a larger/smaller second harmonic absorption profile. However, as long as the modulation depth and cell temperature are maintained, the full width at half maximum (FWHM) has been observed to be largely unaffected.

3.3 Water Vapor Concentration Measurements [12 cm path]

For this portion of the experiment, the 12 cm heated test section and the DFB laser centered at 1491 nm were employed. During each scan the laser was swept across the target wavelength five times at a frequency of 20 Hz, producing a total scan time of 250 ms. The laser was modulated at a frequency of 30 kHz in order to employ a lock-in time constant of 1 ms. The received signal was averaged on-the-fly to produce the desired second harmonic profiles with a reasonable degree of accuracy.

Figures 11A, B, and C depict a compilation of second harmonic absorption profiles obtained using test cell temperatures of 60, 80, and 100°C respectively, and partial pressures of water vapor ranging from 0.042 to 0.380 atm. This corresponds to a test cell relative humidities ranging from roughly 10 % to 80 %. Test cell exhaust temperatures were measured to fall within

18

2°C of the cell temperature. Using the graph for the 80°C cell temperature, it can be seen that the intensity of the absorption peak increases as the partial pressure measured approaches 0.1 atm and begins to decrease beyond this value. In the partial pressure domain beyond 0.247 atm, the signal strength becomes noticeably decreased. This is the result of the formation of condensation on the test cell windows. Because of the differing thermal properties between the aluminum of the cell wall and the BK7 material used for the windows, along with the method of construction and the fact that no heat was directly applied to the glass, the windows were found to be approximately 10°C cooler than the rest of the cell. This lead to condensation forming at lower partial pressure levels than expected. Similar trends were observed for test cell temperatures of 60°C and 100°C.

In order to experimentally observe the effect of cell temperature on the desired measurements, several graphs were constructed comparing similar partial pressure measurements for each of the three temperatures. These graphs can be seen in Figure 12A-D. Four partial pressures (0.056, 0.095, 0.122, and 0.197 atm) were selected to depict the entire range of the experiment. It can be observed that, while there is a distinct change in peak height, the FWHM values for each of the peaks are quite similar. This is especially true for the smaller values of partial pressure. This suggests that, over the relatively small range of temperatures common to operational PEM fuel cells, temperature will not have a large impact on measurement values. This is important as the temperature distribution throughout the cell may vary spatially, depending on the operating conditions. Knowing that the impact of temperature is small, it would not be necessary to create calibration curves for all involved temperatures or means to switch between curves. Rather, a calibration curve would only need to be generated for some average operational value.

Given the parabolic nature of the peak intensities, as well as their dependence upon a large number of variables, they are clearly not the ideal choice for a calibration parameter. Figure 13 displays results relating the FWHM of the absorption profiles for each temperature condition to the partial pressure of water vapor being supplied. It can be seen that at partial pressure values below 0.2 atm the relationship is linear and practically identical for each case. This is expected as FWHM values for such absorption profiles are largely unaffected by temperature variation. At higher partial pressures, the profiles are seen to diverge slightly from their expected linear trend. This is thought to be the result of some unexpected occurrence (such as condensation or two phase flow) in the supply line to the test section.

After the calibration curve had been established, a number of measurements were taken using randomly supplied partial pressures to mimic conditions in an operating fuel cell. Half-width data from these measurements was interpreted using the calibration curve and the results were compared to the known partial pressure being supplied. Some of the data generated has been included in Figure 13. These points have been labeled 'Test' in order to differentiate them from the points used in the calibration. A strong agreement between the test data and calibration curve can be observed, with average error values falling within 5 %. A similar trend was observed for the other measurements as well.

3.4 Water Vapor Concentration Measurements [12 mm pathLength, Direct Pass]

For this portion of the experiment, a single channel heated test cell was used which had been constructed so that the 12 mm depth of the channel was optically accessible (refer to Figure 1). The laser and photodiode were angled in such a way that etalon interference (generated by

20

reflection of the laser off the surface of the optically accessible material) was minimized. During each scan, the laser was swept across the target wavelength five times at a frequency of 10 Hz, producing a total scan time of 500 ms. The laser was modulated at a frequency of 5 kHz in order to employ a lock-in time constant of 5 ms. The received signal was averaged on-the-fly to produce the desired second harmonic profiles.

The second harmonic profiles observed for a cell wall temperature of 80°C and partial pressures of water vapor ranging from 0.042 to 0.380 atm can be seen in Figure 14A. It can be seen that the intensity of the absorption peak increases as the partial pressure measured approaches 0.1 atm and begins to decrease beyond this value. Because of the homogeneous composition of the materials used in the construction of the cell (acrylic) and the direct application of heat to the sections being optically accessed, condensation did not occur at any relative humidity below 100 %. In order to observe the formation of condensate and its effect upon the measurement, the partial pressure of water vapor was increased until saturation was achieved. An image of the observed droplets can be seen in Figure 15. It is interesting to note that the formation of condensation did not have a significant impact on the strength of the signal. Similar measurements were also taken using a cell wall temperature of 60°C and identical trends were observed.

Given the parabolic nature of the peak intensities, was well as their dependence upon a large number of variables, they are clearly not the ideal choice for a calibration parameter. Figure 14B displays the relationship between the FWHM and partial pressure values for both temperature conditions used with the 12 mm path length. We see a solid agreement between the two datasets and a nearly linear trend. This is expected as FWHM values for such absorption profiles are largely unaffected by temperature variation. After generating the calibration curve a

21

number of random measurements were taken and comparison was made between the calibrated values and supplied values. It was observed that these values were comparable with an average error of less than 5 %.

3.5 Water Vapor Concentration Measurements [12 Mm pathlength, MEA Scattering Calibration]

For the next portion of the experiment, two single channel optically accessible plates similar to the one described in the previous section were assembled with an MEA between them in order to simulate a fuel cell flow channel (refer to Figure 2A). To create a reliable calibration curve, it was necessary to take some measure to prevent water transport across the membrane. For this reason, a sheet of laminate material which was observed to be transparent in the near-IR spectrum was inserted between the MEA and the humid flow channel. Humid air from the humidifier was supplied at known partial pressures and measurements were taken by shining the laser upon the surface of the MEA at an angle. A high gain photodiode was strategically placed in order to capture some of the backscattered radiation. The placement of the photodiode was such that any reflection of the laser off of the acrylic window or laminate sheet was avoided. During the generation of the calibration curve, the laser was swept twenty times at a frequency of 2 Hz for a total scan time of 10 s. The beam was modulated at 5 kHz and a lock-in time constant of 5 ms was employed. The observed second harmonic profiles were again the result of on-the-fly averaging.

The calibration curve generated in this exercise can be seen in Figure 16. The expected linear trend is once again observed. It should be noted that this calibration curve differs from the

one generated for the direct pass measurements. This is the result of the increased scan time and photodiode gain. Though the backscattered measurements were somewhat 'nosier' than those gathered previously, a reasonable repeatability error was observed, with values falling within 10% of those expected.

3.6 Water Vapor Concentration Measurements [12 Mm pathlength, Water Transport]

In order to observe the water vapor transport across the membrane, the laminate sheet added for the previous section was removed from the test section. Humid air from the humidifier was supplied to one channel while dry heated air was supplied to the other. During the course of this experiment, the flow rates of both channels were maintained at 2 lpm. Again, light from the laser was shone upon either surface of the MEA at an angle and the photodiode was placed to gather some of the scattered radiation. For each measurement, the laser was swept ten times at a frequency of 2 Hz for a total scan time of 5 s. Modulation and time constant settings were the same as those for the previous section. Again, the received signal was averaged on-the-fly to produce the desired second harmonic profiles.

In order to validate the measurement technique, measurements were first taken along the humid channel while heating the test section to avoid any condensation (refer to Figure 2B). It was expected that, under these conditions, the observed half widths of the second harmonic profiles would be similar to those seen in the previous section with some consideration given for moisture loss due to transport across the MEA. The measured half-widths can be seen in Figure

8. At low partial pressures, FWHM values deviate from the linear trend and tend to exhibit a non-linear decay.

After ensuring the validity of the technique, the heating elements were removed from the test section to allow for the air entering the humid channel to reach a state of super-saturation (refer to Figure 2C). Measurements were taken at the center of both channels (I and II) for various amounts of supplied partial pressure. Figure 17 compares the observed water vapor partial pressure values for these measurements as obtained using the calibration curve shown in Fig. 16. When the calibration curve is applied, the partial pressures of water vapor on the dry (I) and humid (II) sides are shown to range between ambient-0.048atm and 0.200-0.312atm respectively. The dry side is supplied with ambient air at 25 C with a relative humidity of 50 %. A slight partial pressure increase from this ambient value is observed to take place on the dry side of the cell as the supplied humidity on the humid side is increased to large values. This is the result of species transport across the porous MEA. It should be noted that the measured humidity on the humid side of the cell displays substantial deviation from the expected supplied values. This deviation is much greater to be accounted for by species transport alone. This is most likely the result of the large amount of observed condensation (as droplets) in the gas channels and water absorption by the MEA.

A good degree of repeatability was observed, with error values within 10%. It should be noted that the measurements on the humid side were obtained through the condensation (see Figure 18), showing that the technique can be implemented even under two-phase flow conditions. While it has been previously noted that such measurements are possible, the observed signal became noisier as the levels of condensate increased suggesting a greater

24

scattering of the laser light. Such conditions would require more averaging and thus longer scan times to ensure accuracy.

3.7 Carbon Dioxide Concentration Measurements [12 cm pathlength]

For the final portion of the experiment, the 12 cm test section was used. As the effect of cell temperature upon FWHM values is minimal and there was no need to maintain a high temperature to prevent condensation, the cell was kept at room temperature. Volumetric flow rates of carbon dioxide and air were controlled by rotameters and mixed in specified proportions in a tank. The gas mixture was then passed through the test section and scanned using a laser centered at 1570.4 nm. The scans were conducted using a sweep frequency of 4 Hz, a modulation frequency of 5 kHz, and a lock-in time constant of 5 ms. A total of ten scans per measurement were employed, resulting in a total measurement time of 2.5 s.

Figure 19A show the set of second harmonic absorption profiles generated using various partial pressures of carbon dioxide ranging from 0.111 atm to 1 atm. A second graph (Figure 19B) displays profiles ranging in carbon dioxide concentration from 0.015 atm to 0.111 atm. Peak intensity can be seen to increase steadily along with greater CO_2 concentrations, especially in the high concentration regime. At lower concentrations, a greater uncertainty in supplied gas volumes could have produced the sporadic increases in peak intensity, though it was also noted that signal intensity drops off rapidly at concentrations less than 0.055 atm.

The plot of FWHM vs. concentration of carbon dioxide (Figure 11C) appears predominantly linear in the region beyond 0.055 atm. Below this value, the curve drops off rapidly as the absorption profile is buried in signal noise. It would be very difficult to establish a

25

reliable calibration curve for these regions given the relatively short path length. However, 1-2 % percentage changes in species concentration could be measured accurately in the regions beyond 0.055 atm concentration.

CHAPTER FOUR: CONCLUSIONS

Calibration curves for measuring the partial pressure of water vapor and the species concentration of carbon dioxide along relatively short path lengths were established using wavelength modulation spectroscopy. The technique utilizes a laser modulated at a high frequency in order to measure the absorption properties of a species when the absorption profile might otherwise be lost within the base signal noise. This allows for concentration measurements to be made across short path lengths and small time spans, a requirement when seeking to monitor something such as species transport within PEM fuel cells during high load cycles.

Using controlled flow conditions, the chosen absorption peaks for water vapor and carbon dioxide were shown to be valid and repeatable. Though the intensity of the absorption profiles might vary with changes in alignment or gain, the full widths at half maximum were observed to remain unaffected. The direct and first harmonic absorption profiles for the water vapor transition (located at 1491.6 nm) were compared to those generated mathematically for the same transition using data from the most recent HITRAN database. The profiles matched to a high degree, further validating the method of measurement.

For the second harmonic profiles of water vapor absorption along both path lengths (12 cm and 12 mm) the peak intensities were seen to increase until the supplied partial pressure reached approximately 0.1 atm. After this point, the peak intensity began to decrease, but the profiles continued to broaden. A comparison of the FWHM values to the partial pressure of water vapor showed a predominantly linear relationship, especially in the lower partial pressure regions. Random measurements taken to assess the validity of the observed relationship deviated

by less than 5 % on average from the calibration curves. Test section temperature was observed to have very minimal impact on these curves at low partial pressure values. Total scan times of 250 ms and 500 ms were employed for the 12 cm and 12mm cases, respectively. These relatively short scan times would make application of this measurement process ideal for dynamic environments such as operational PEM fuel cells under high frequency load cycles. As some of the dynamic processes which take place in an operating PEM fuel cell have been reported to occur with temporal resolutions less than 0.15 s [35], it should be noted that scan times can be decreased at the cost of a slightly larger measurement error. Using the parameters set forth in this report, on-the-fly averaging could be removed from the measurements, resulting in scan times as low as 0.05 s. This has been observed experimentally to produce an error closer to 15 %.

When the MEA was introduced into the 12 mm path length, the results of measuring the backscattered radiation revealed similar linear trends to those observed for earlier water vapor measurements. The technique was used to monitor the humidity on either side of the MEA during both temperature controlled and super-saturated conditions. These measurements demonstrated the ability of the MEA to transport water vapor, with observable loss increasing with greater supplied partial pressures. The measurements were observed to be repeatable to within 10%. The successful use of the measurement system proved that the technique could be useful to gather more localized data along PEM fuel cell flow channels.

The carbon dioxide profiles were shown to increase in peak intensity along with increasing CO_2 concentration. This increase was observed to be relatively steady in the regions beyond 10%. A comparison of the profile FWHM values and the concentration also showed a linear relationship beyond this point. Below 10%, the absorption peak dropped off rapidly,

28

becoming lost in the noise of the signal. Given the small path length it would be fairly difficult to generate any kind of reliable calibration curve within this region. Barring this, the calibration curve allowed for small changes (~1-2%) to be observed in the regions above 10 % CO2 concentration. A total scan time of 2.5 s was employed for this measurement.

Though these measurements were conducted using test paths with relatively small aspect ratios, the technique could easily be ported for use in mini-channel applications. The only limitations on channel width and depth are imposed by the size of collimated laser beam. In future work this method will be applied to a specially designed PEM fuel cell flow plate.

APPENDIX: FIGURES
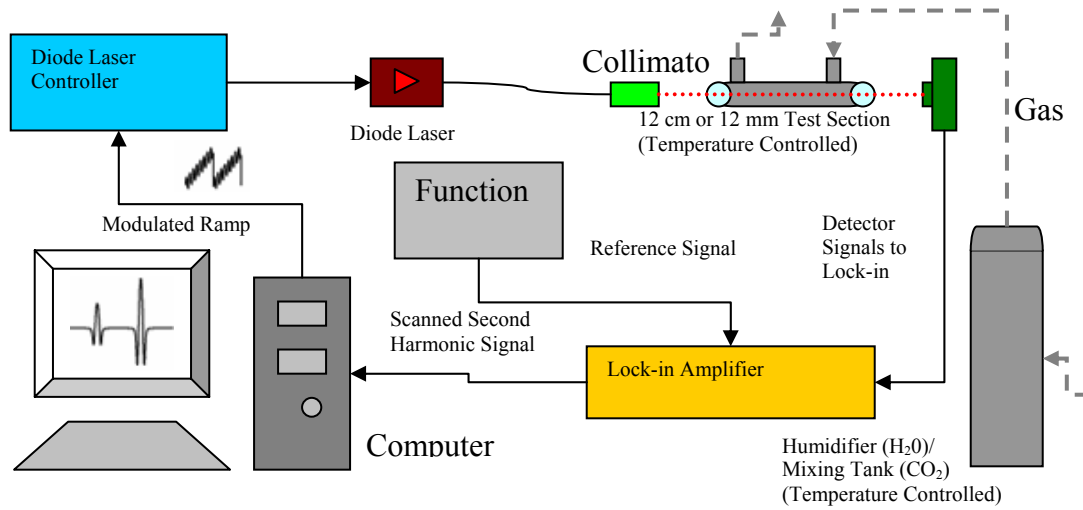
Figure 1: Experimental setup and WMS flow diagram. (Adapted from [32])
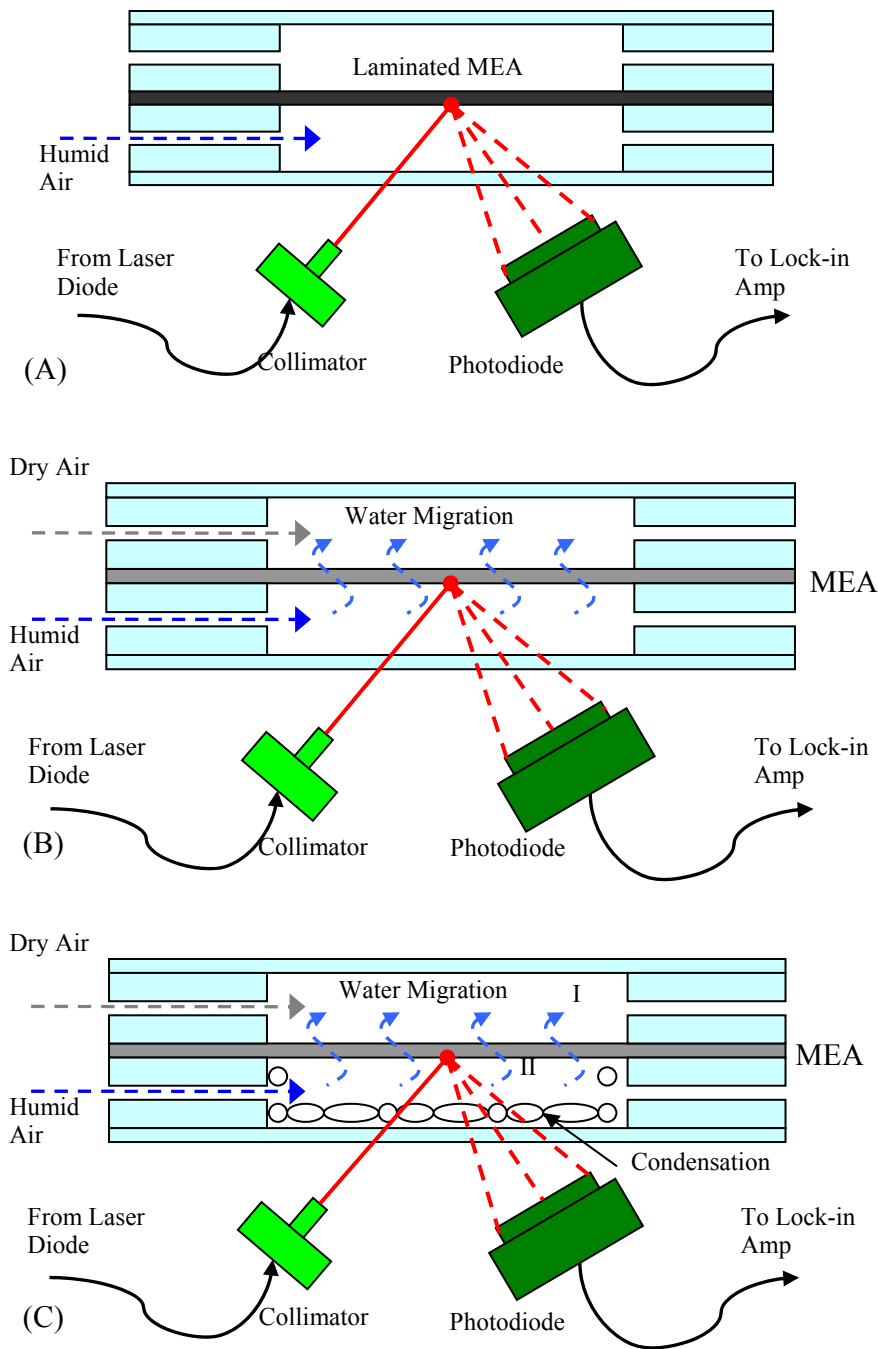
Figure 2: Cross sectional diagrams of the test section used in the MEA backscatter portion of the experiment. (A) A laminate sheet was placed in front of the MEA to prevent water transport across the membrane. (B) The cell in this image has been heated to prevent condensation in order to verify the measurement technique. (C) Measurements were taken for both the dry air (I) and humid air (II) sides under unheated and super-saturated conditions to measure water vapor transport across the MEA.

32
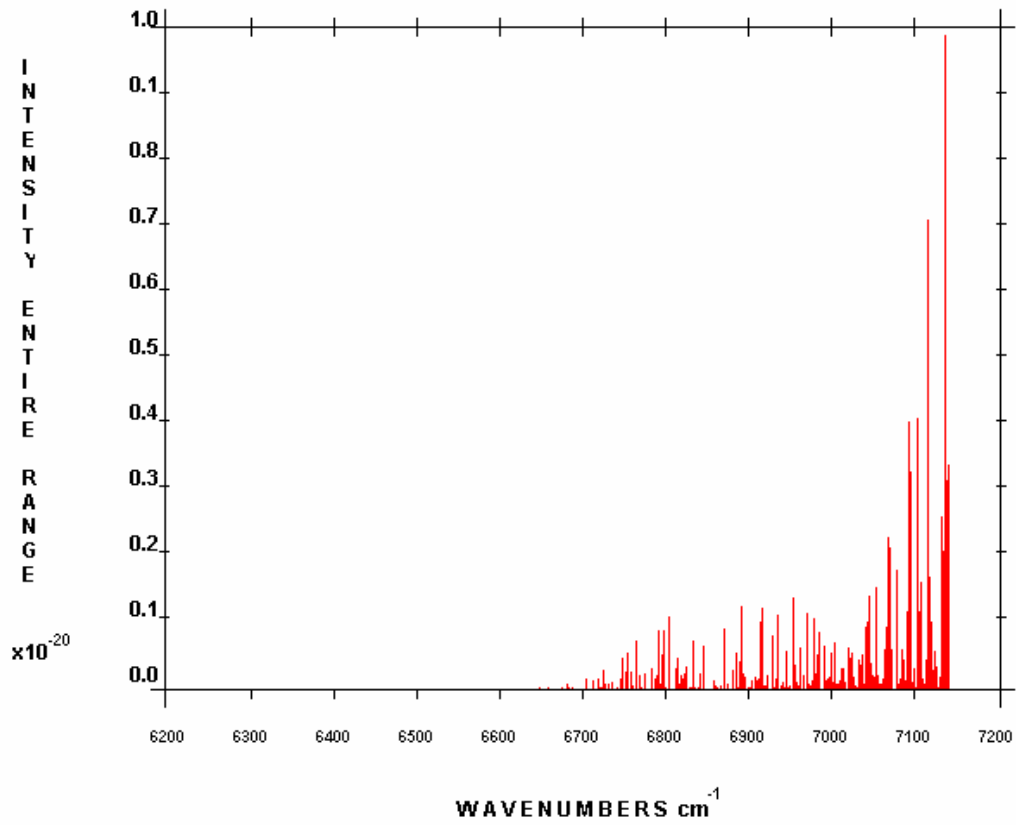
Figure 3: A bar graph depicting the absorption intensities for existing transitions for water vapor in the near-ir spectral range from 1400 to 1600 nm
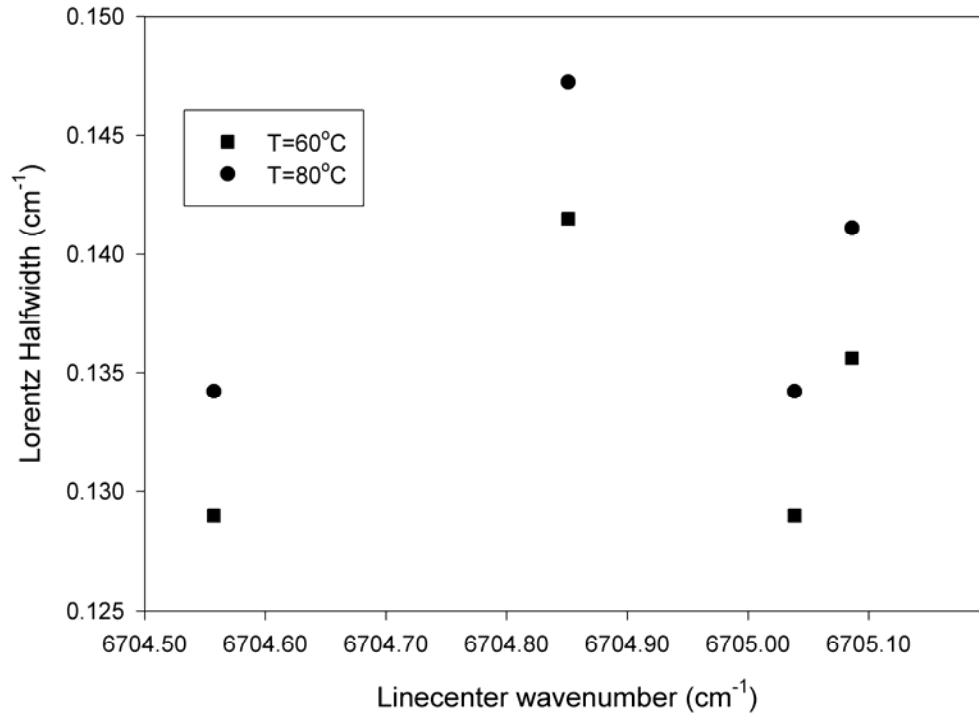
Figure 4: HITRAN simulations for the Lorentz halfwidth of the direct absorption caused by a single partial pressure of water vapor at various temperatures across the 1491.416 transition. The variation of Lorentz halfwidth with temperature is about 2.2% compared to the 38% variation with partial pressure.
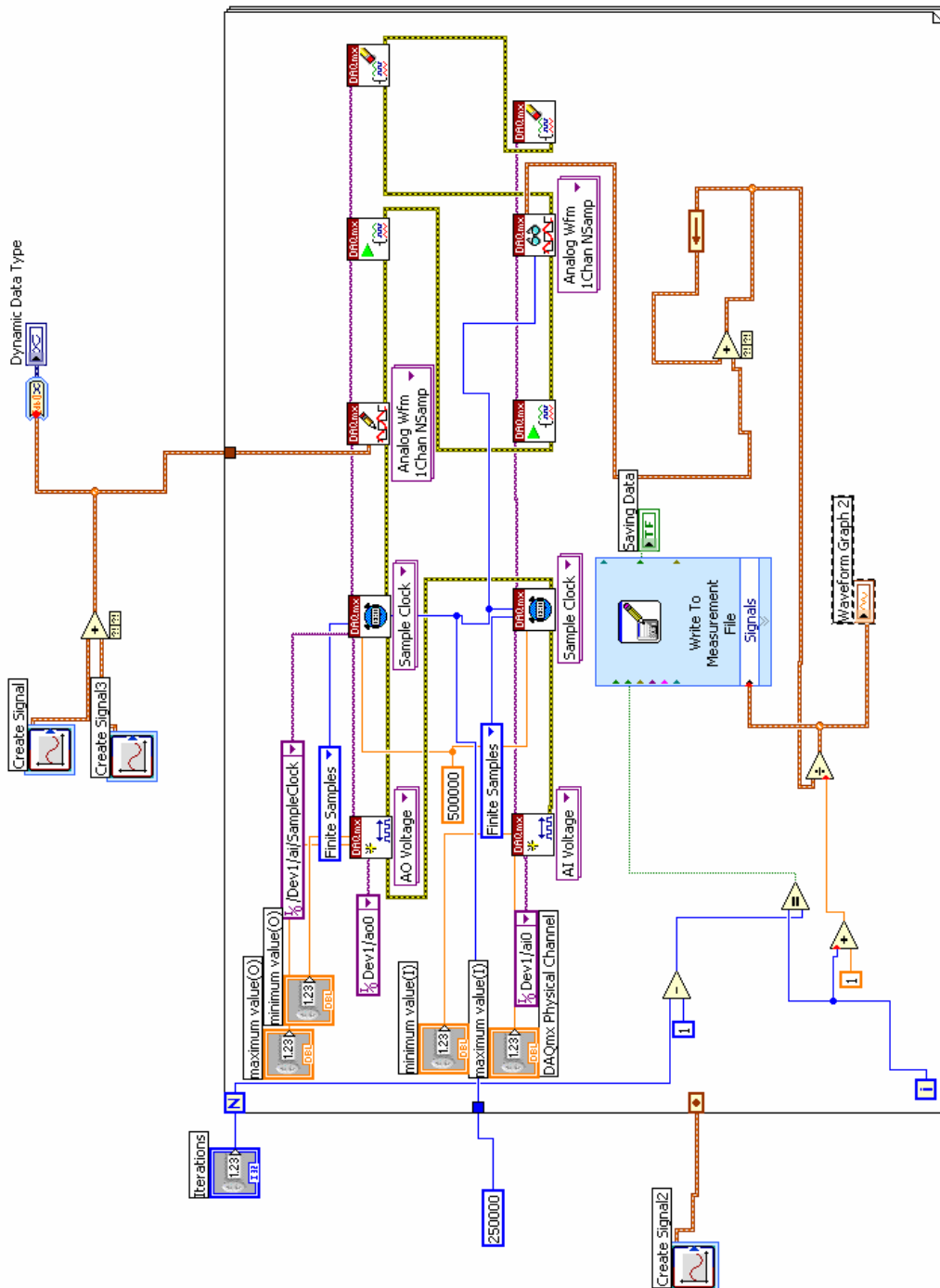
Figure 5: A block diagram of the LabView program used to control the laser and gather data throughout the course of the study.
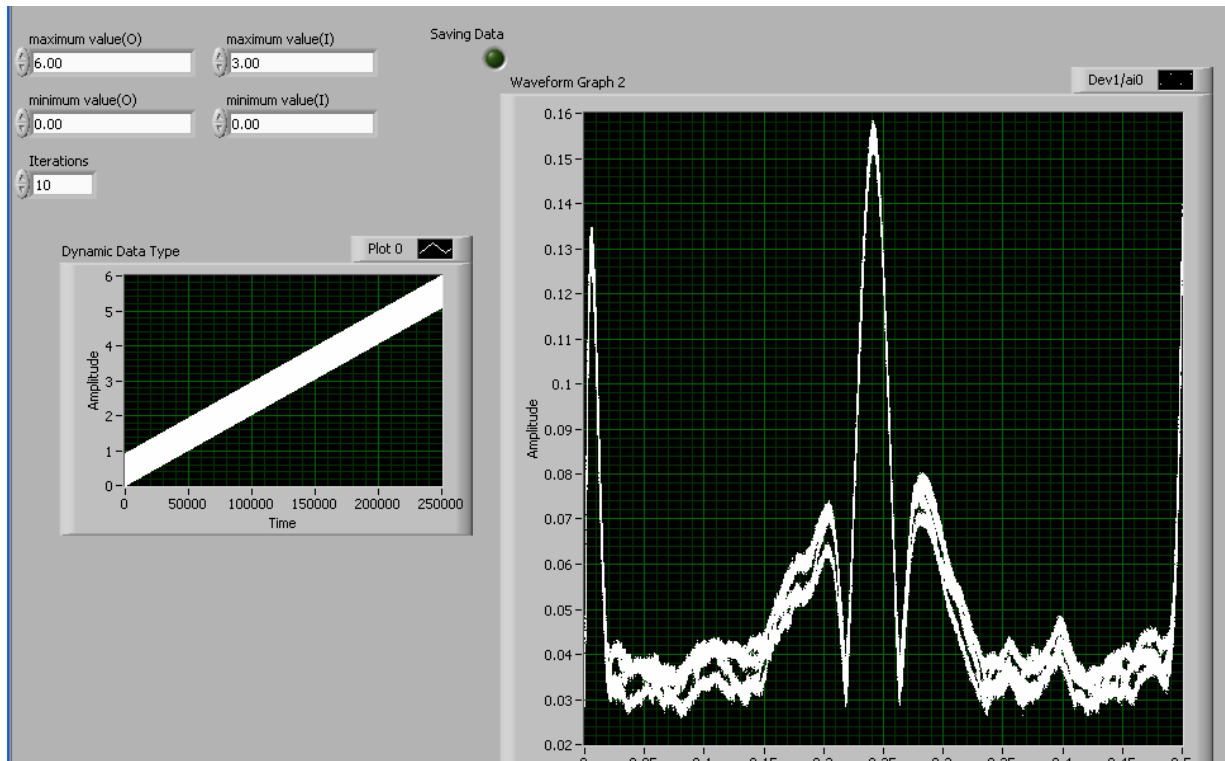
Figure 6: A screenshot of the control pannel for the LabView program used to obtain measurements during the study. User controls for input and output values are seen in the upper left hand corner. The graph immediately below displays the output to the laser controller while the larger graph shows the obtained input.

Figure 7: A block diagram of the LabView program used to measure the FWHM of recorded second harmonic absorptions.

www.manaraa.com
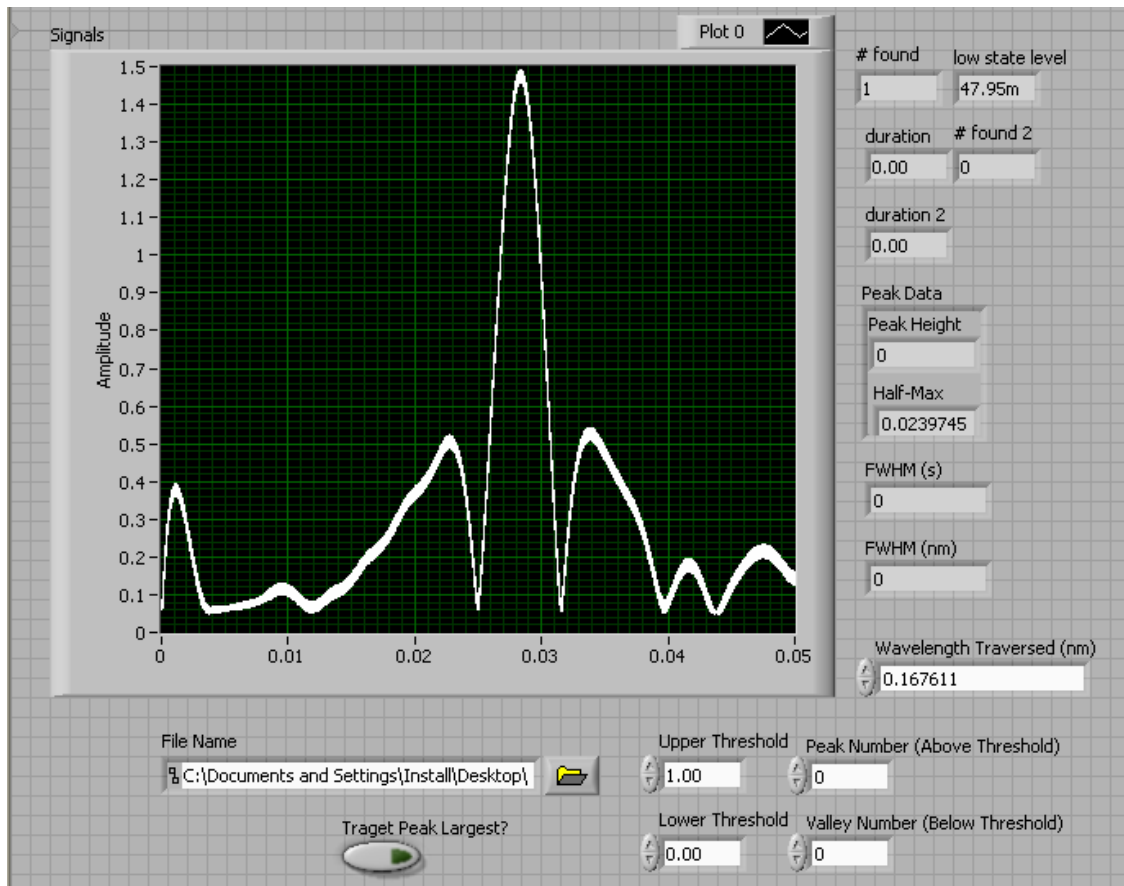
Figure 8: A snapshot of the front pannel for the LabView program used to measure the FWHM values. User controls for setting the desired measurement file and profile characteristics are found along the bottom. A graph of the data is also displayed along with various values of interest.
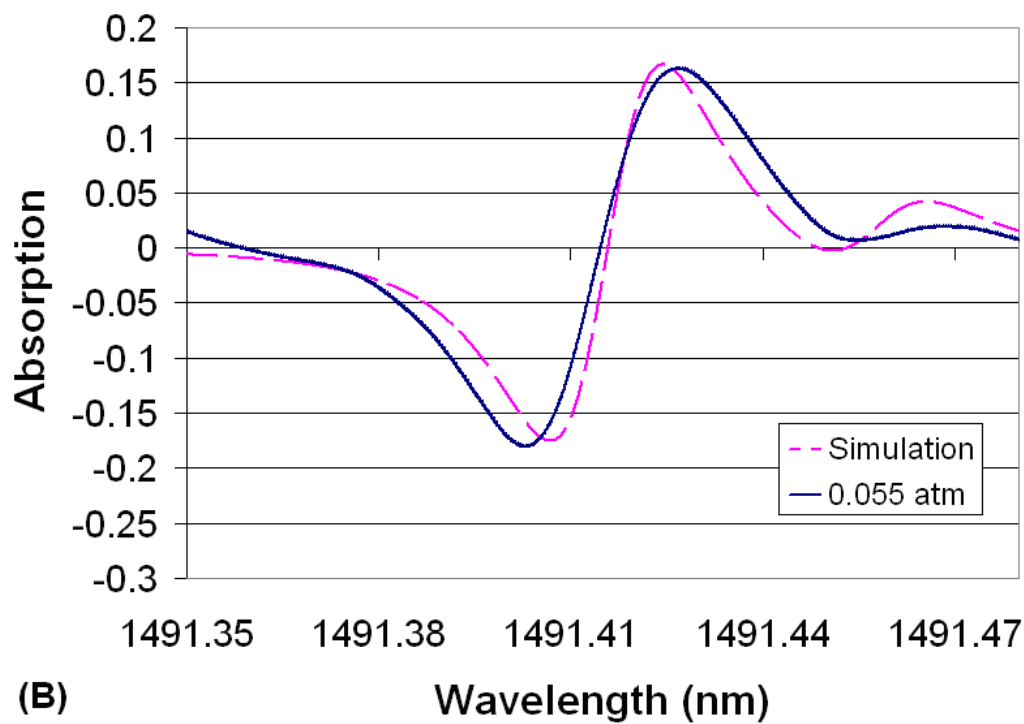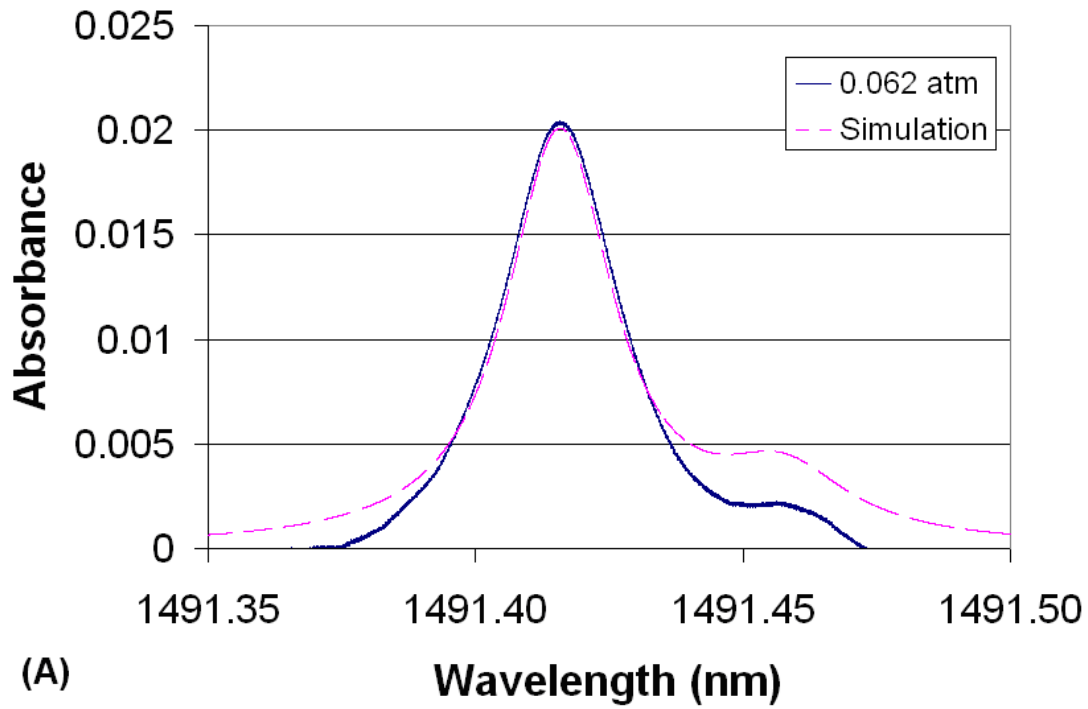
Figure 9: Graphs comparing the (A) direct and (B) first harmonic absorption profiles for water vapor with HITRAN based simulations.
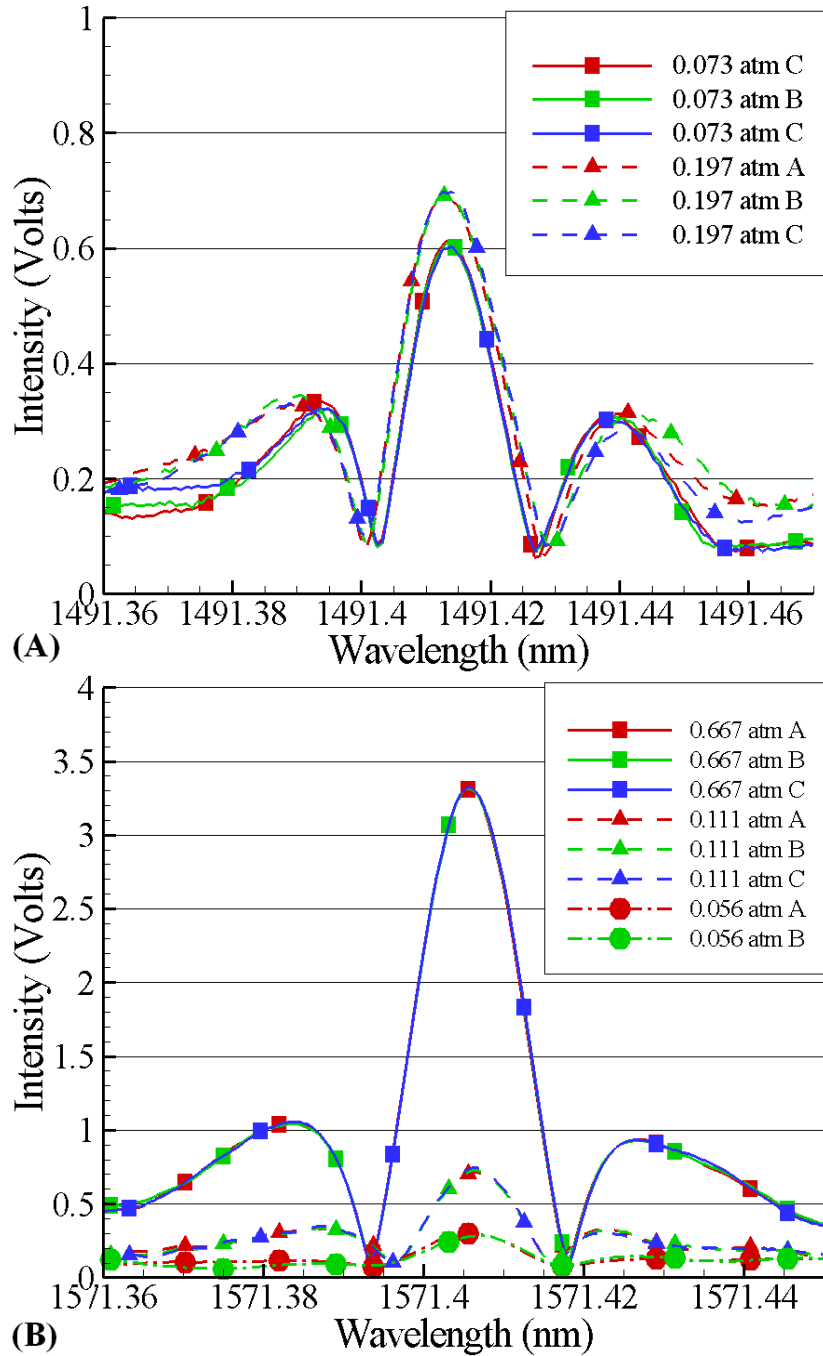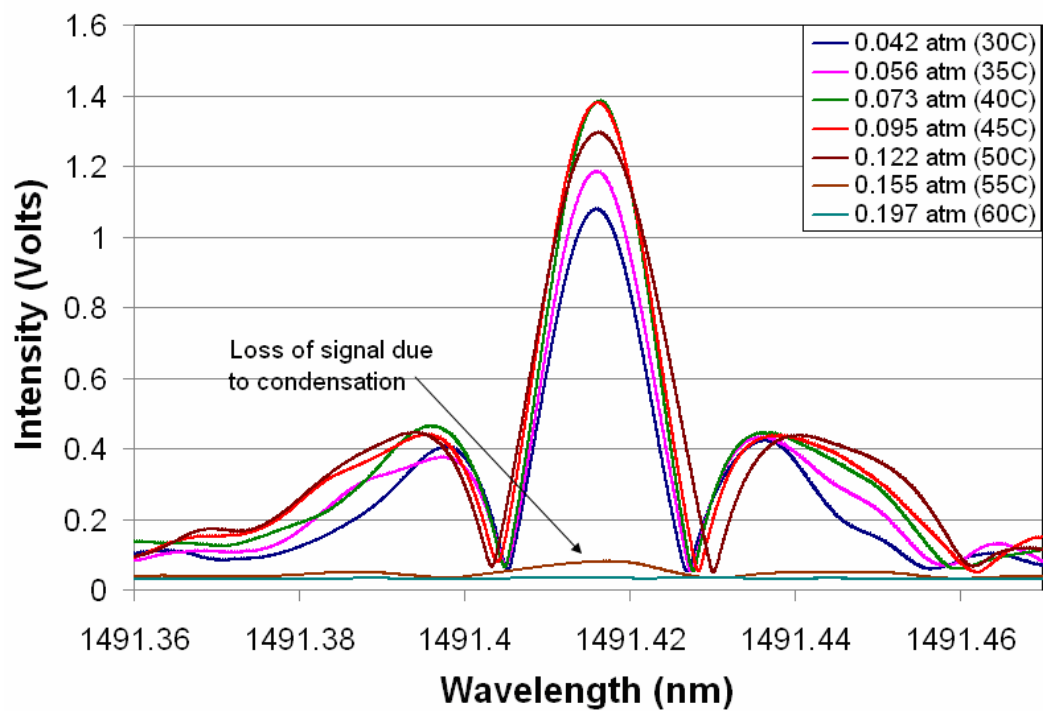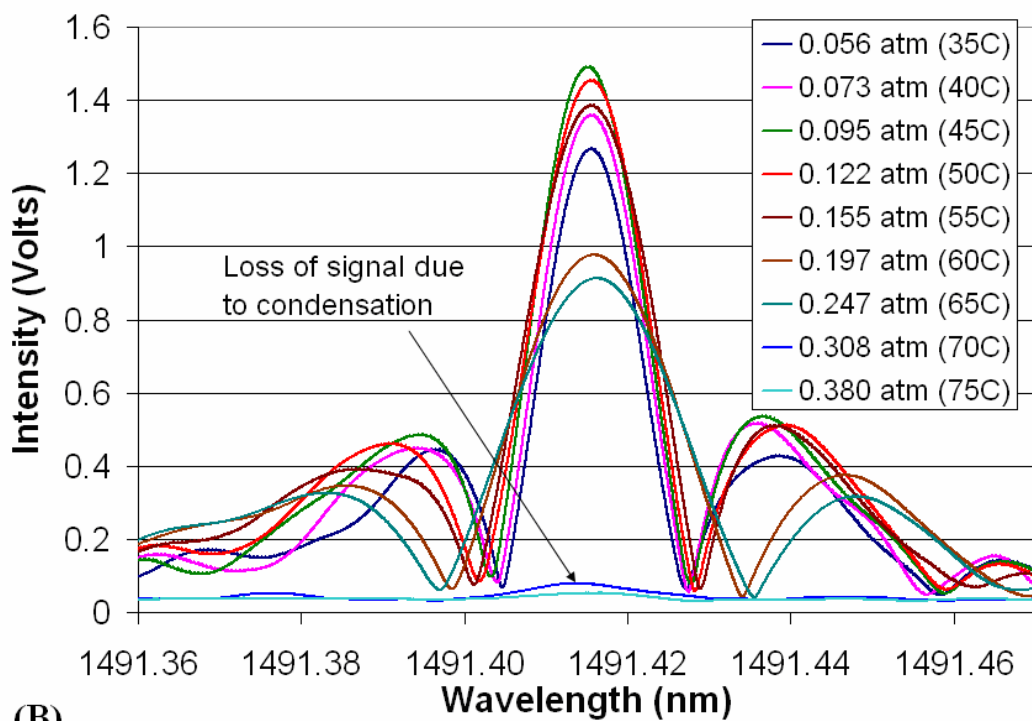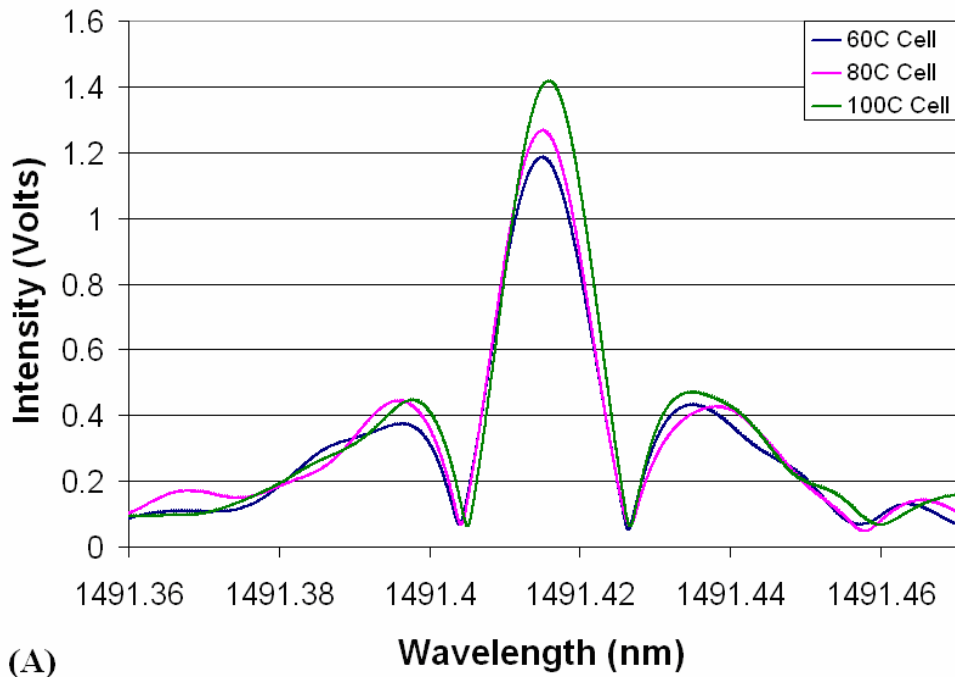
Figure 10: Repeatability profiles for (A) water vapor measurements across the 12 mm test cell, and (B) carbon dioxide measurements along the 12 cm test cell.
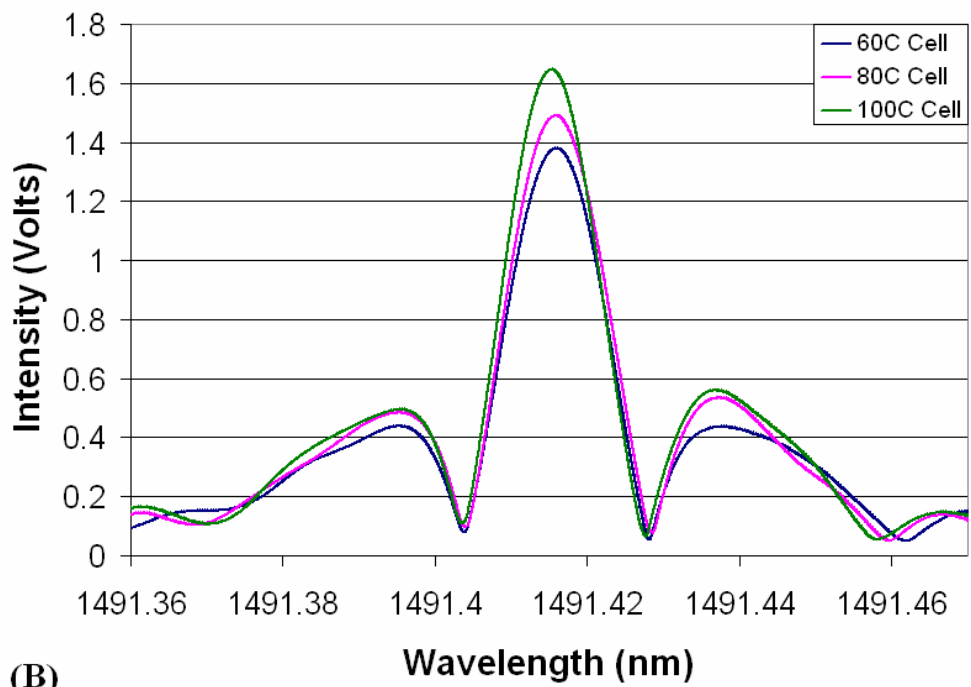
(A)

(B)

41

Figure 11: Graphs depicting the progression of the second harmonic absorption profiles for increasing partial pressure of water vapor in a 12cm test cell at (A) 60°C, (B) 80°C, and (C) 100°C.
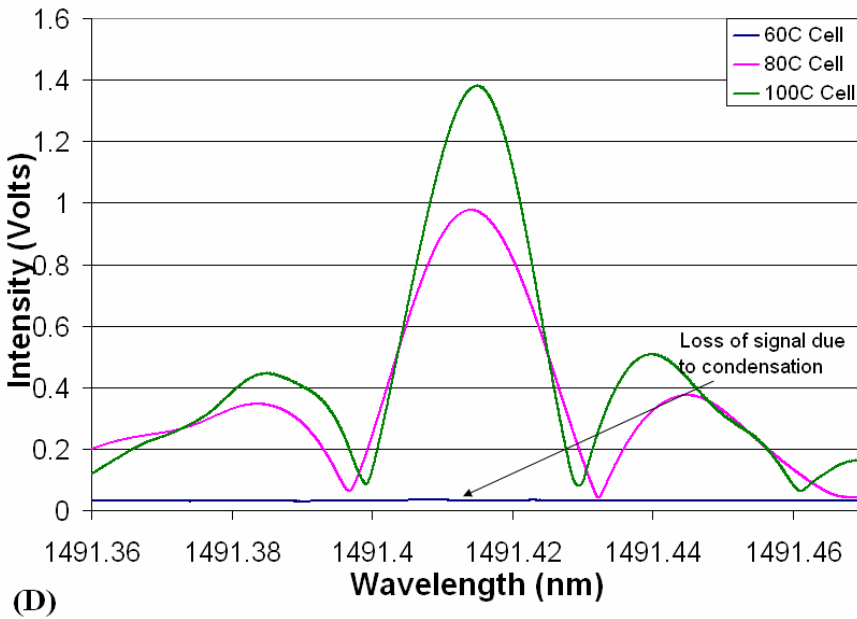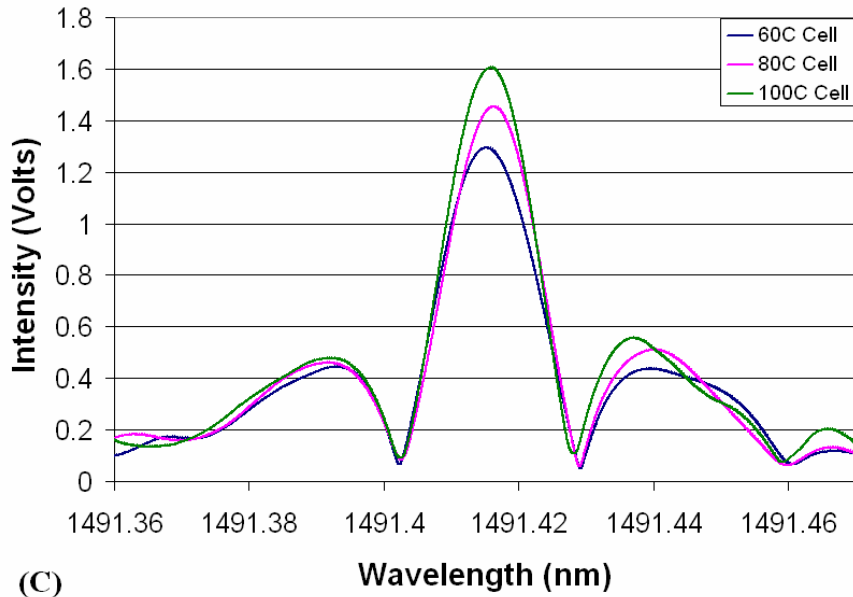
(A)

(B)

43

Figure 12: Graphs displaying the effect of temperature variation of the test cell. Each graph displays the 2f profiles for 60°C, 80°C, and 100°C. The supplied partial pressures include (A) 0.056 atm, (B) 0.095 atm, (C) 0.122 atm, and (D) 0.197 atm.
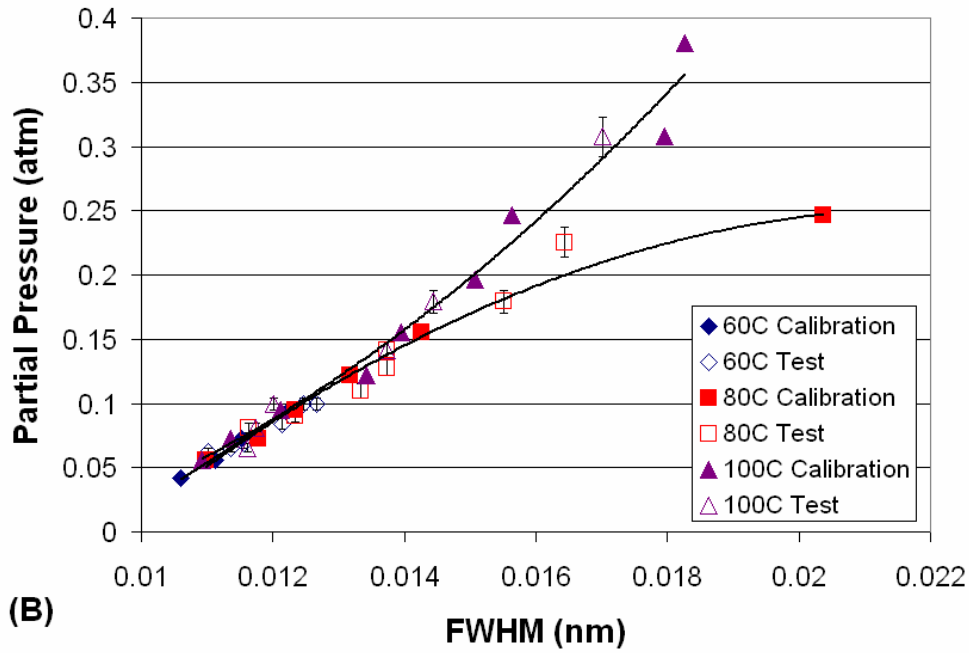
44

Figure 13: Calibration curve for determining the partial pressure of water vapor using the FWHM of the second harmonic absorption profile.
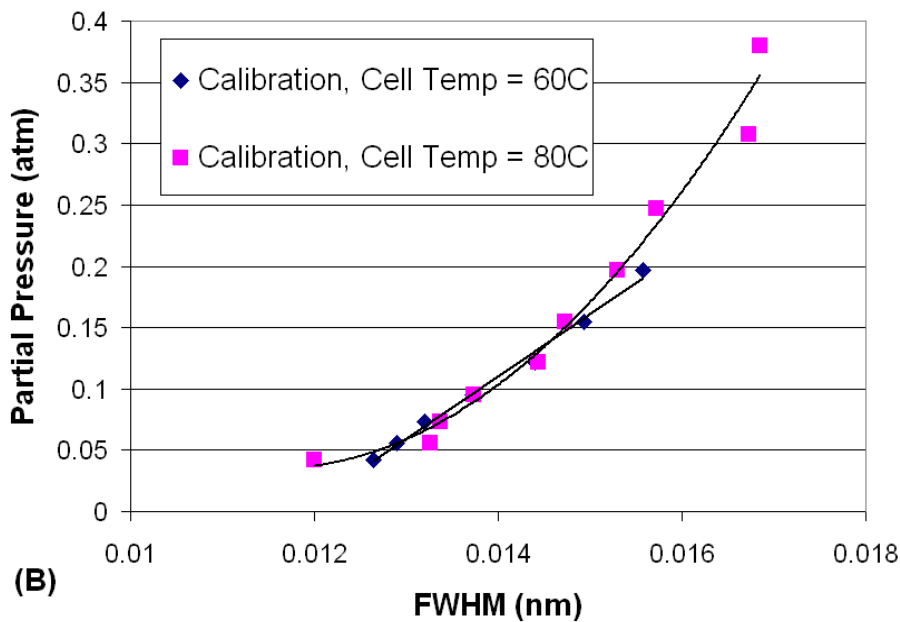
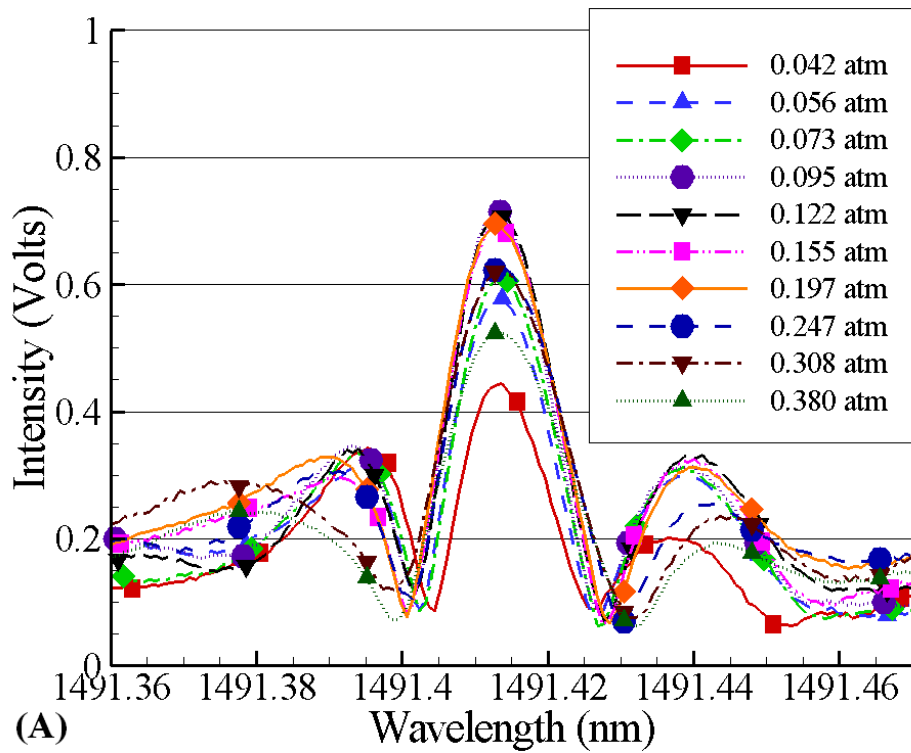Figure 14: (A) A graph depicting the progression of the second harmonic absorption profiles for increasing partial pressure of water vapor in a 12mm test cell at 80°C. (B) Calibration curve for determining the partial pressure of water vapor using the FWHM of the second harmonic absorption profile.
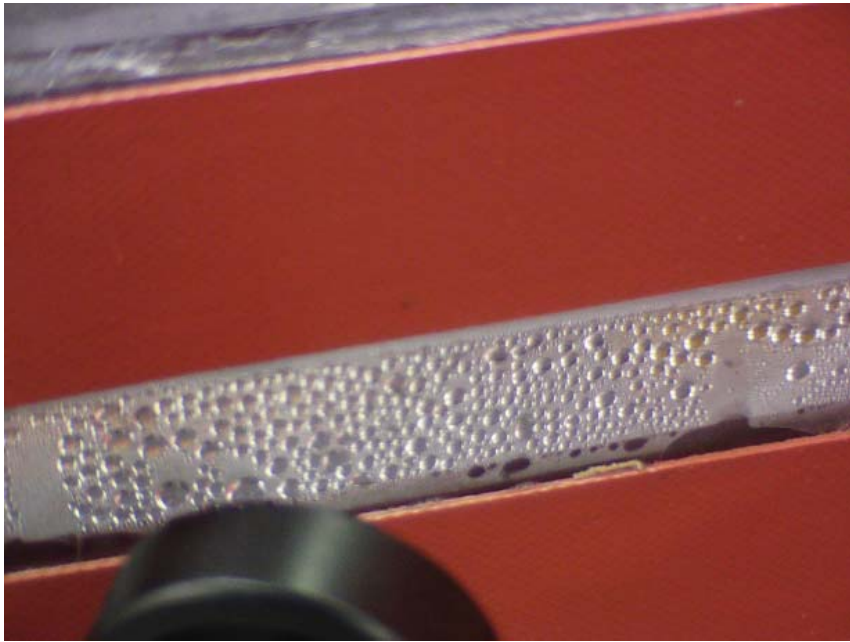
46

Figure 15: A photograph displaying the formation of condensation along the walls of the 12mm heated test cell.
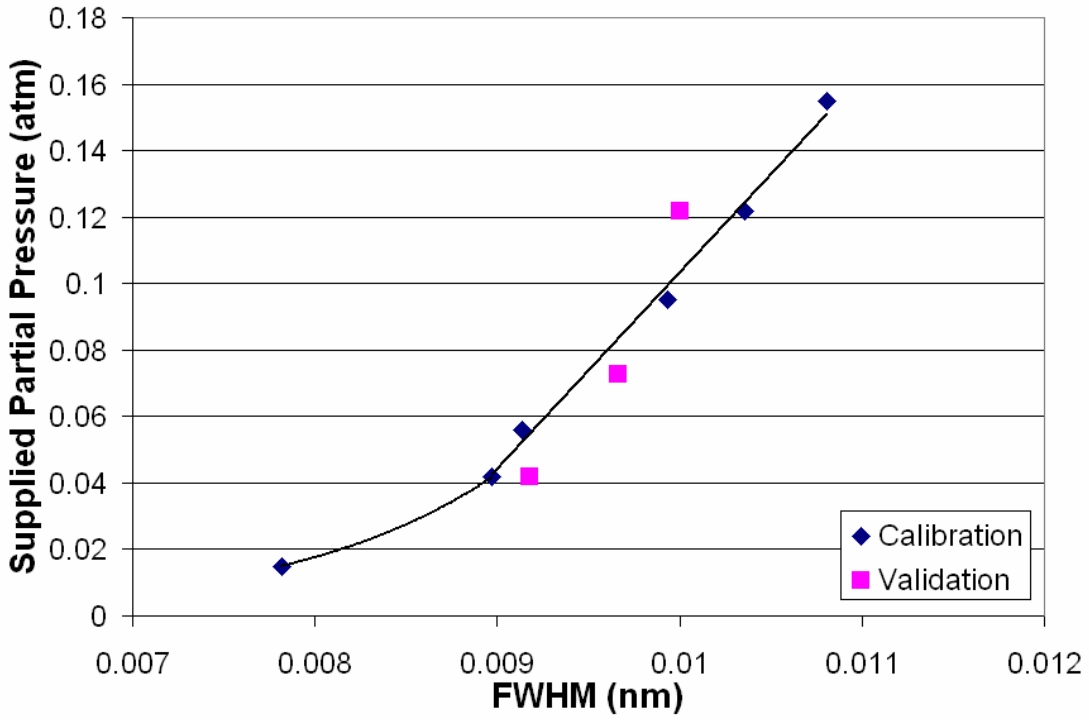
Figure 16: A graph depicting the calibration curve generated for the MEA backscatter measurements (ref Fig. 2A) as well as the validation measurements gathered in the heated test section (ref Fig. 2B).
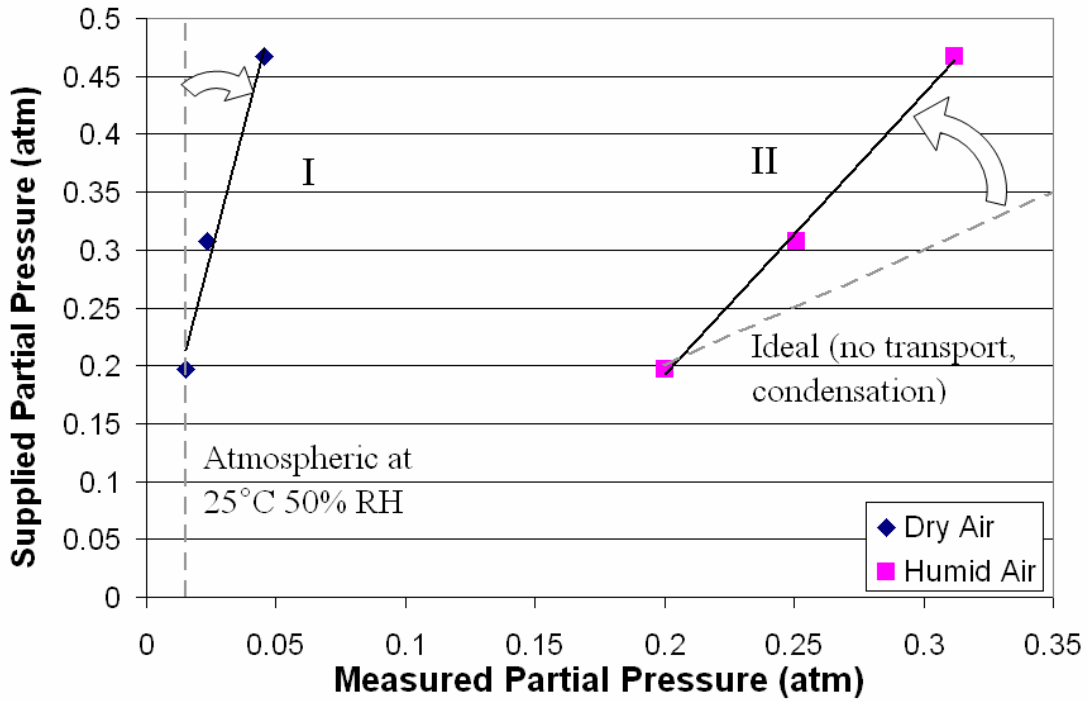
Figure 17: A graph depicting the observed water vapor partial pressure values for a super-saturated cell (ref Fig. 2C) on both the dry (I) and humid (II) sides of the MEA. Increase on the dry side is due to species transport across the MEA while the loss on the humid side is predominantly due to condensation.
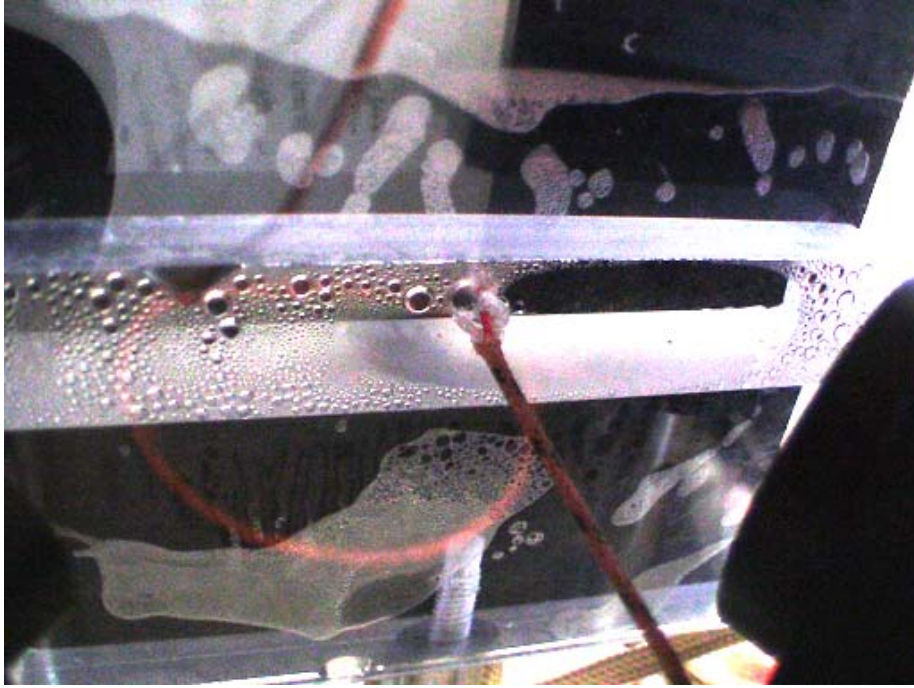
Figure 18: An image displaying the condensation which was occurring in the humid flow channel during the super-saturated MEA backscatter measurements.

(A)

(B)

51
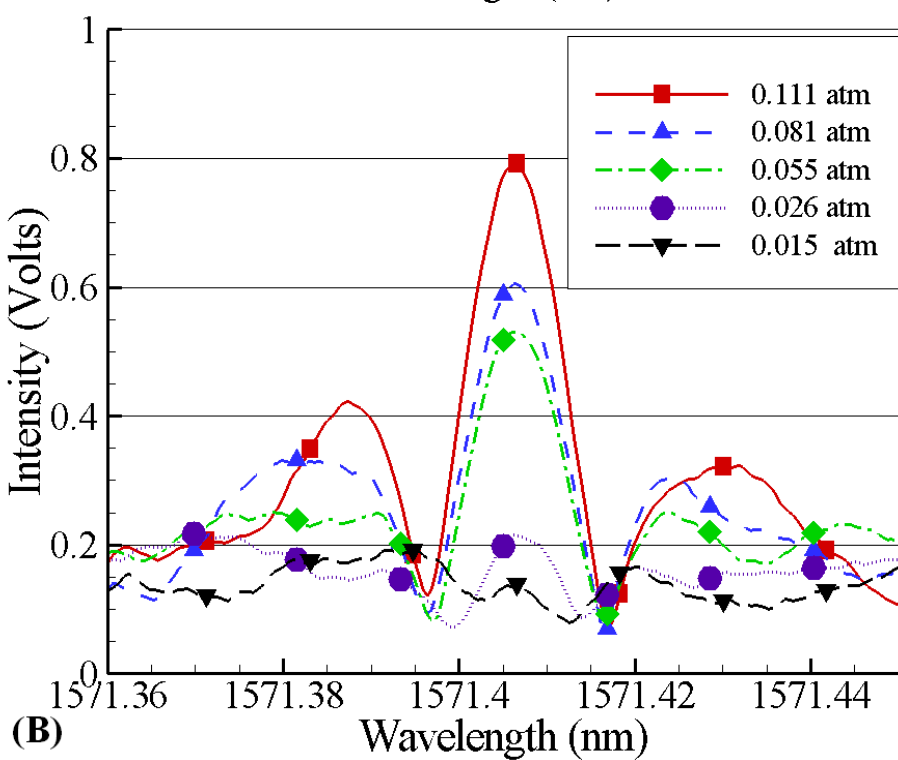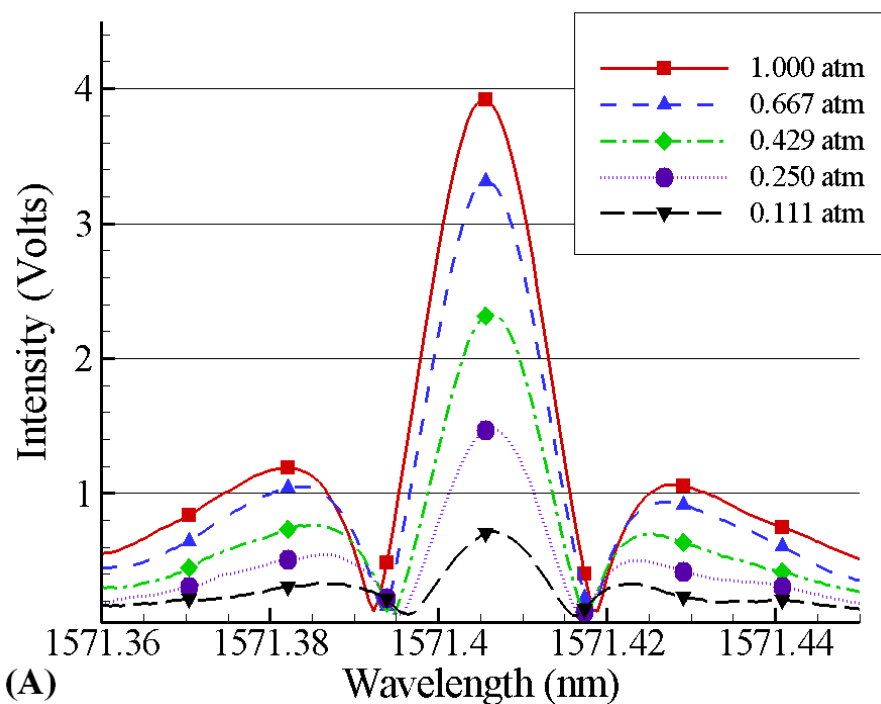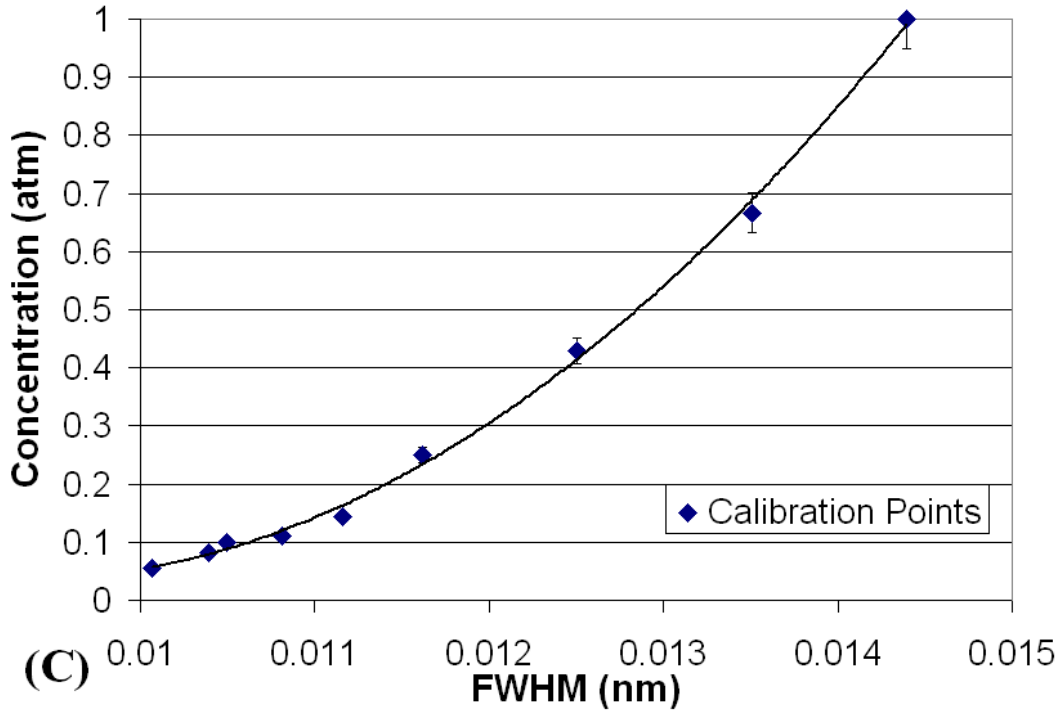
Figure 19: (A) A graph depicting the progression of the second harmonic absorption profiles for increasing concentration of carbon dioxide in a 12cm test cell at room temperature with values greater than 0.111 atm. (B) A second absorption profile progression graph for carbon dioxide partial pressures less than 0.111 atm. (C) Calibration curve for determining the concentration of carbon dioxide using the FWHM of the second harmonic absorption profile at partial pressures greater than 0.055 atm.

APPENDIX: TABLES

Table 1: A table displaying the HITRAN values for absorption intensity of water vapor transition lines in the spectral range from 1491-1492 nm. Yellow highlight depicts chosen transition while green indicates other transitions included in laser sweep.

H2O Transitions

Wavenumber (cm^-1)	Wavelength (nm)	Absorption Intensity
6702.5021	1491.980137	6.22E-25
6702.81186	1491.911187	8.38E-26
6702.96897	1491.876219	7.06E-24
6703.09682	1491.847764	2.45E-25
6703.23946	1491.816018	5.59E-25
6703.25664	1491.812195	4.38E-25
6703.28476	1491.805937	8.02E-26
6703.36828	1491.78735	6.47E-26
6703.43708	1491.772039	3.00E-25
6703.46935	1491.764858	1.60E-24
6703.68168	1491.717608	4.46E-25
6703.87825	1491.673868	1.75E-25
6704.11778	1491.620572	1.52E-26
6704.16478	1491.610115	8.26E-27
6704.55736	1491.522775	5.52E-23
6704.8509	1491.457476	2.89E-23
6705.03851	1491.415744	1.63E-22
6705.08746	1491.404856	8.29E-25
6705.23959	1491.371019	1.61E-26
6705.67274	1491.274685	2.58E-26
6706.1083	1491.177827	2.47E-26
6706.47673	1491.095907	1.14E-25
6706.8106	1491.021679	6.33E-26

Table 2: A table displaying the HITRAN values for absorption intensity of carbon dioxide transition lines in the spectral range from 1571-1572 nm. Yellow highlight depicts chosen transition while green indicates other transitions included in laser sweep.

CO2 Transitions

Wavenumber (cm^-1)	Wavelength (nm)	Absorption Intensity
6361.570857	1571.938791	4.28E-27
6361.597176	1571.932287	4.19E-25
6361.7021	1571.906361	7.42E-27
6362.056637	1571.818764	1.01E-26
6362.265358	1571.767199	4.69E-25
6362.322396	1571.753108	7.62E-27
6362.444762	1571.722879	4.74E-26
6362.504303	1571.708171	1.74E-23
6363.055439	1571.572037	5.13E-25
6363.083502	1571.565106	1.05E-26
6363.2388	1571.526751	7.93E-27
6363.679951	1571.417808	5.53E-25
6363.691089	1571.415058	4.32E-26
6363.728118	1571.405914	1.64E-23
6363.814523	1571.384578	1.31E-26
6364.398058	1571.240502	5.10E-27
6364.488582	1571.218154	5.86E-25
6364.571936	1571.197576	1.54E-26
6364.7788	1571.14651	8.25E-27
6364.911592	1571.113731	3.86E-26
6364.922481	1571.111043	1.51E-23
6365.063381	1571.076265	6.14E-25
6365.279524	1571.022916	1.75E-26

LIST OF REFERENCES

[1] S.G. Kandlikar, Fundamental issues related to flow boiling in minichannels and microchannels, Experimental Thermal and Fluid Science 26 (2-4) (2002) 389-407.

[2] R. Jeschar, H. Kraushaar H. Griebel, Influence of gases dissolved in cooling water on heat transfer during stable film boiling, Steel Research 67 (6) (1996) 227–234.

[3] Q. Cui, S. Chandra, S. McCahan, Enhanced boiling of water droplets containing dissolved gases or solids, in: Proceedings of 34th National Heat Transfer Conference, Pittsburgh, PA, Paper No. NHTC2000-12249, 2000, pp. 1–12.

[4] M. E. Steinke, S. G. Kandlikar, Control and effect of dissolved air in water during flow boiling in microchannels, International Journal of Heat and Mass Transfer 47 (8-9) (2004) 1925-1935.

[5] A.Y. Tonkovich, J.L. Zilka, M.J. LaMont, Y. Wang, R.S. Wegeng, Microchannel reactors for fuel processing applications. I . Water gas shift reactor, Chemical Engineering Science 54 (13-14) (1999) 2947-2951.

[6] A.H. Epstein, Millimeter-Scale, Micro-Electro-Mechanical Systems Gas Turbine Engines, Journal of Engineering for Gas Turbines and Power 126 (2) (2004) 205-226.

[7] L.G. Fre´chette, S.F. Nagle, R. Ghodssi, S.D. Umans, M.A. Schmidt, J.H. Lang, An electrostatic induction micromotor supported on gas-lubricated bearings, in: Proceedings of IEEE 14th International Micro Electro Mechanical Systems Conference, Interlaken, Switzerland, 2001, pp. 1-4.

[8] A. Deux, Design of a Silicon Microfabricated Rocket Engine Turbopump, M.S. thesis, MIT Department of Aeronautics and Astronautics, MIT, Cambridge, MA. 2001.

[9] G. Alberti, M. Casciola, L. Massinelli, B. Bauer, Polymeric proton conducting membranes for medium temperature fuel cells (110-160°C), Journal of Membrane Science 185 (1) (2001) 73–81.

[10] J. Larminie, A. Dicks, Fuel Cell Systems Explained, Wiley, New York, 2000.

[11] P. Costamagna, S. Srinivasan, Quantum jumps in the PEMFC science and technology from the 1960s to the year 2000: Part II. Engineering, technology development and application aspects, Journal of Power Sources 102 (1-2) (2001) 253–269.

[12] F.A. de Bruijn, D.C. Papageorgopoulous, E.F. Sitters and G.J.M. Janssen, The influence of carbon dioxide on PEM fuel cell anodes, Journal Power Sources 110 (1) (2002) 117-124.

[13] A. Collier, H. Wang, X.Z. Yuan, J. Zhang, D.P. Wilkinson, Degradation of polymer electrolyte membranes, Journal of Hydrogen Energy 31 (13) (2006) 1838-1854.

[14] A. Faghri, Z. Guo, Challenges and opportunities of thermal management issues related to fuel cell technology and modeling, International Journal of Heat and Mass Transfer 48 (19-20) (2005) 3891-3920.

[15] P.W. Li, T. Zhang, Q.M. Wang, L. Schaefer and M.K. Chyu, The performance of PEM fuel cells fed with oxygen through the free-convection mode, Journal of Power Sources 114 (1) (2003) 63–69.

[16] D. Natarajan and T.V. Nguyen, A Two-Dimensional, Two-Phase, Multicomponent, Transient Model for the Cathode of a Proton Exchange Membrane Fuel Cell Using Conventional Gas Distributors, Journal of the Electrochemical Society 148 (12) (2001) A1324–A1335.

[17] P.T. Nguyen, T. Berning, N. Djilali, Computational model of a PEM fuel cell with serpentine gas flow channels, Journal of Power Sources 130 (1-2) (2004) 149–157.

57

[18] S. Um and C.Y. Wang, Three-dimensional analysis of trenaport and electrochemical reactions in polymer electrolyte fuel cells, Journal of Power Sources 125 (2004) 40–51.

[19] T. Berning and N. Djilali, A 3D, multi-phase, multicomponent model of the cathode and anode of a PEM fuel cell, Journal of the Electrochemical Society 150 (12) (2003) A1589–A1598.

[20] Q. Dong, J. Kull, M.M. Mench, Real-time water distribution in a polymer electrolyte fuel cell, Journal of Power Sources 139 (1-2) (2005) 106–114.

[21] M.M. Mench, Q.L. Dong, C.Y. Wang, In situ water distribution measurements in a polymer electrolyte fuel cell, Journal of Power Sources 124 (2003) 90–98.

[22] I. Tkach, A. Panchenko, T. Kaz, V. Gogel, K.A. Friedrich, E. Roduner, Electrochemical difference between anodes in Direct Methanol Fuel Cells and polished/single crystal model electrodes, Physical Chemistry Chemical Physics 6 (2004) 5419–5426.

[23] D.J. Beaubien, The chilled mirror hygrometer: how it works, where it works—and where it doesn't, Sensors Magazine 22.5 (2005) 30–34.

[24] D. Kramer, J. Zhang, R. Shimoi, E. Lehmann, A. Wokaun, K. Shinohara, G.G. Scherer, In situ diagnostic of two-phase flow phenoment in polymer electrolyte fuel cells by neutron imaging Part A: Experimental, data treatment, and quantification, Electrochimica Acta 50 (2005) 2603–2614.

[25] R. Satija, D.L. Jacobson, M. Arif, S.A.Werner, In situ neutron imaging to evaluate water management systems in operating PEMFCs, Journal of Power Sources 129 (2) (2004) 238–245.

[26] J.P. Owejan, T.A. Trabold, D.L. Jacobson, M. Arif, S.G. Kandlikar, Effects of flow field and diffusion layer properties on water accumulation in a PEM fuel cell, International Journal of Hydrogen Energy 32 (17) (2007) 4489-4502.

[27] V.R. Albertini, B. Paci, A. Generosi, S. Panero, M.A. Navarra, M. di Michiel, In Situ XRD Studies of the Hydration Degree of the Polymeric Membrane in a Fuel Cell, Electrochemical and Solid State Letters 7 (12) (2005) A519–A521.

[28] J. Borrelli, J. Owejan, T. Trabold, S.G. Kandlikar, Water Transport Visualization and Two-Phase Pressure Drop Measurements In a Simulated PEMFC Cathode Minichannel, in: Proceedings of 3rd International Conference on Microchannels and Minichannels, Toronto, Canada, (2005) p ICMM2005-75118.

[29] S. Basu, H. Xu, M.W. Renfro, B.M. Cetegen, In-situ optical diagnostics for measurements of water vapor concentration and temperature in PEM fuel cell, ASME Journal of Fuel Cell Science and Technology 3 (2006) 1–7.

[30] S. Basu, G. Haluk, M.W. Renfro, B.M. Cetegen, In-situ Simultaneous Measurements of Temperature and Water Partial Pressure in a PEM Fuel Cell under Steady State and Dynamic Cycling, Journal of Power Sources 159 (2006) 987–994.

[31] S. Basu, M.W. Renfro, B.M. Cetegen, Spatially-resolved optical measurements of water partial pressure and temperature in a PEM fuel cell under dynamic operating conditions, Journal of Power Sources 162 (2006) 286-293.

[32] J.T.C. Liu, J.B. Jeffries, R.K. Hanson, Wavelength Modulation Absorption Spectroscopy with 2f Detection using Multiplexed Diode Lasers for Rapid Temperature Measurements in Haseous Flows, Applied Physics B 78 (2004) 503-511

[33] Y. Fujii, S. Tsushima, S. Hirai, Investigation of Current Density Effect on Water Vapor Concentration Profile along PEMFC Channels by TDLAS, Journal of Thermal Science and Technology 3 (2008) 94-102

[34] S. Schilt, L. Thevenaz, P. Robert, Wavelength Modulation Spectroscopy: Combined Frequency and Intensity Laser Modulation, Applied Optics 42 (33) (2003) 6728-6738.

[35] S. Pischinger, C. Schonfelder, J. Ogrzewalla, Analysis of dynamic requirements for fuel cell systems for vehicle applications, Journal of Power Sources 154 (2006) 420-427